A Satellite Synthetic Aperture Radar Concept Using *P*-Band Signals of Opportunity

Simon H. Yueh ⊙ , *Fellow, IEEE*, Rashmi Shah ⊙ , *Senior Member, IEEE*, Xiaolan Xu ⊙ , Bryan Stiles, and Xavier Bosch-Lluis ⊙

Abstract—The spaceborne aperture radar (SAR) technique based on a combination of *P*-band signals of opportunity (SoOp) reflectometry with a sparse array of receivers at low earth orbits (LEOs) and transmit signals from the United States Navy's Mobile User Objective System operating on a geosynchronous altitude has been analyzed. The design focuses on the forward-looking geometry near the specular direction, which allows a high surface reflectivity, in order to obtain adequate signal-to-noise ratio (SNR) with a moderate receiving antenna gain. The sparse array is utilized to sharpen the across-track resolution and reduce the iso-range ambiguity. The formulation for match filtering and illustrations of point target response are presented. This work shows that an array of five to seven receivers is able to achieve an across-track resolution of about 200 m in the outer portion of swath and about 1 km in the center part of swath. The along-track resolution can reach 10 m or better due to the feasibility of a long dwell time for Doppler filtering. We find that the sparse array allows the reduction of the iso-range ambiguity to a level of lower than 5% for a major portion of swath, ~70% or greater depending on the number of receivers and spacing. We have completed an SNR formulation, which can consistently account for both coherent and incoherent scattering regardless the spatial resolution. An analysis of SNR based on the Kirchhoff approximation for rough surface scattering has been performed. We find that it is possible to obtain a swath width of 100 km with an SNR of 5 dB or better for a constellation of seven satellites with a receiving antenna directivity of 15 dBi at a LEO altitude of 675 km for a wide range of surface roughness. Our study suggests the promise of the SoOpSAR concept for high-resolution remote sensing of land surfaces.

Index Terms—Bistatic radar, *P*-band, signals of opportunity (SoOp), snow, soil moisture, synthetic aperture radar (SAR).

I. INTRODUCTION

HIGH-RESOLUTION (a few hundred meters) remote sensing of root zone soil moisture (RZSM) and snow water equivalent (SWE) is critical for modeling of land surface hydrological processes and applications to water resource management, precision farming, and flood monitoring. SWE is the effective water depth should the snow completely melt away. Despite their importance, SWE and RZSM are two of the least measured hydrologic states in the earth system, in part due to the challenges of required space technologies with large antenna apertures and, hence, large satellites for support.

The current technology for high-resolution remote sensing of RZSM is based on the *P*-band synthetic aperture radar (SAR) technology. A radar mission concept using a 30-m-diameter mesh reflector with phase array feeds was proposed to achieve a spatial resolution of 1 km [1]. The European Space Agency's (ESA's) BIOMASS mission with a swath width of about 50 km and a resolution requirement of 200 m based on the *P*-band SAR technologies will have potential to provide the RZSM [2], [3]. SAR technologies have also been considered for a high-resolution remote sensing of SWE. The satellite mission COld REgions Hydrology High-resolution Observatory (CoReH2O) was assessed by the Earth Explorer Programme of the ESA for an extended phase A study from 2007–2012 [4]. The proposed sensor for CoReH2O was a dual frequency SAR, operating at *Ku*-band (17.2 GHz) and *X*-band (9.6 GHz), VV and VH polarizations, with a swath width of about 100 km and a spatial resolution in the range of 100 to 500 m for various scientific applications. The Airborne Snow Observatory [5], an airborne imaging spectrometer, and a LIDAR can provide a survey of snow depth, but is limited to an airborne platform for regional coverage. Interferometric SAR based on the differential propagation delay of microwave signals through snow has also been demonstrated for high-resolution imaging of SWE at *C*-band frequency [6], *L*-band [7], and *X*-/*K*-band [8]; these frequency bands are much more affected by vegetation cover than *P*-band.

However, the United States (US) Department of Defense has worked with the International Telecommunication Union (ITU) to designate the US Space Objects Tracking Radar as the primary user of the 435-MHz band. This change has restricted future spaceborne *P*-band earth remote sensing radars, such as the ESA's BIOMASS mission [2], [3], from operating over North America and most of Europe.

Signals of opportunity (SoOp) technologies for land and ocean remote sensing have been gaining popularity in the past three decades. The use of global navigation satellite system reflectometry (GNSS-R) signals at *L*-band (L1 = 1.57542 GHz) for surface soil moisture retrieval has been demonstrated by field campaigns [9]–[13]. Demonstration of spaceborne GNSS reflectivity dependence on surface soil moisture has been performed based on TechDemoSat-1 data in [14]–[16], in SMAP-R [17], [18] (at L2 = 1.2276 GHz), and the data from the National Aeronautics and Space Administration Cyclone Global Navigation Satellite System (CYGNSS) mission [19]–[21].

The spatial resolution of GNSS-R is limited by the bandwidths of Doppler shift and GNSS transmit signals [22]. The spatial resolution of CYGNSS or TechDemoSat-1 using onboard processing methods for generation of delay-Doppler map (DDM) can reach a few kilometers if the coherent scattering dominates [23], but will be limited to 20 to 30 km if the incoherent scattering by the surfaces has a more significant contribution [22], [24].

In addition, GNSS signals at *L*-band have limited penetration into soil and forest canopies. A complementary frequency band is the signal from the US Navy's Mobile User Objective System (MUOS), a communication satellite system operating at *P*-band frequencies [25]. There are four operational MUOS satellites at geosynchronous altitudes, providing global land surface coverage. Each satellite broadcasts dual-frequency channels at *P*-band (360–380 MHz and 240–270 MHz).

The use of *P*-band SoOp from MUOS has been receiving increasing attention for soil moisture sensing and other land hydrology elements [26]–[36]. Field experiments and theoretical modeling to test the applicability of *P*-band SoOp for snow water storage and soil moisture have also been investigated. However, *P*-band reflectometry will have the same spatial resolution limitations as the *L*-band GNSS-R, depending on the dominant surface scattering mechanisms, coherent or incoherent [37], [38].

With the objective of achieving a high spatial resolution, regardless of scattering mechanisms, we have completed a study to assess the potential of a low earth orbit (LEO) based receiver constellation concept based on the MUOS transmit signals and the multistatic SAR concept [39], which is applied in our research to address the iso-range ambiguity in the GNSS-R DDM [22], a key issue for the forward-looking geometry.

In this article, we describe the *P*-band SoOp SAR (SoOpSAR) concept in Section II. The constraints on Doppler bandwidth and integration time are discussed in Section III. A parametric performance is presented to illustrate the spatial resolution, iso-range ambiguity level, and signal-to-noise ratio (SNR) in Section IV. We analyzed the characteristics of MUOS signals, in particular to determine the potential effects of range ambiguities due to a certain temporal repeatability of MUOS coding in Section V. Two key technology issues related to timing of signal detection and formation flights are discussed in Section VI. A summary is given in Section VII.

II. SoOpSAR Concept

The SoOpSAR, operating near the specular reflection direction for maximal SNR, can be combined with a sparse array of receivers to achieve a high spatial resolution, a reduced ambiguity level, and an improvement in SNR (see Fig. 1). Using multiple receivers flying in formation offers the possibility for the differentiation of true target location and its ambiguity.

For simplicity of the concept illustration, we let $\phi = 0°$ in Fig. 2. For the receiver moving with a velocity of v along the *x*-axis, the ambiguous position of a target located at (x_c, y_c) is $(x_c, -y_c)$, indicated by the red open circle in Fig. 2. Even after the receiver has moved by vt along the *x*-axis, the ambiguity stays at the same position in y although the dimension of iso-range
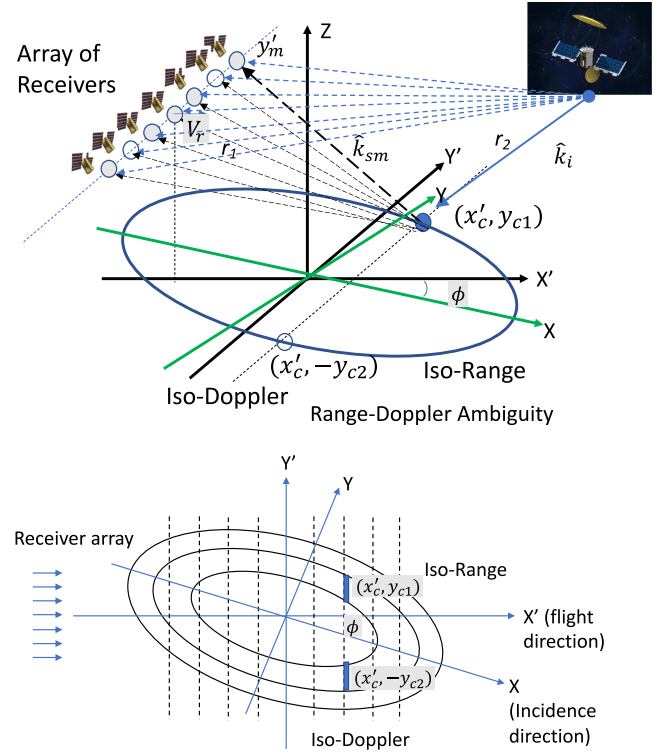

Fig. 1. SoOpSAR concept based on a sparse array of receivers to detect reflected signals from the MUOS. The flight direction is off the incidence plane by an angle ϕ in azimuth. (Upper) an illustration of incidence and receiving geometry; $\hat{k}_i$ is the unit vector for incident wave from transmit satellite; $\hat{k}_{sm}$ is the unit vector of reflected signal toward the *m*th receiver. (Lower) a projection on the horizontal plane with inclusion of iso-range and Doppler contours. Range compression and Doppler filtering will lead to a pair of location ambiguities (blue slices).
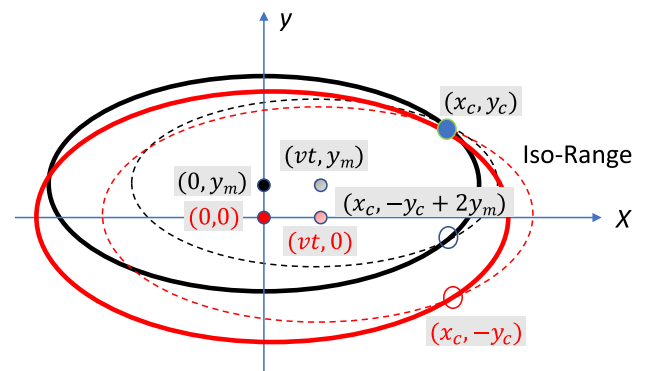

Fig. 2. Ambiguities of signals from two receivers appear in different locations. The case of $\phi = 0°$ is illustrated here. The iso-range contours are located by solid lines for receivers at time $= 0$ s. After time $= t$, the receivers with a velocity of v have moved by vt and the dimension of iso-range contours indicated by dashed lines has changed.

contours has changed (solid red line versus dashed red line). For the other receiver located at $(0, y_m)$ and also moving in parallel to the *x*-axis, the ambiguous position is $(x_c, -y_c + 2y_m)$, indicated by the black open circle. As shown, the ambiguities in the signals received by the two receivers are offset from each other by $2y_m$ along the *y*-axis. If the relative phase difference between the reflected signals from the ambiguity $(x_c, -y_c)$ into two
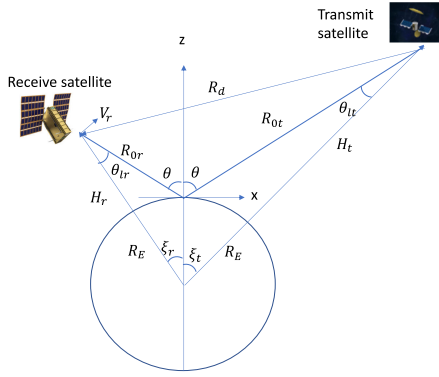
Fig. 3.　Geometry of SoOp radar.

receivers is close to 180°, then we can use the signals from two receivers to isolate the target by coherently combining signals from two receivers to suppress the ambiguity. However, some target locations cannot be distinguished from their ambiguities when the relative phase difference is close to 0°, same as the signal from the target. Introducing an array of receivers will then allow the reduction of ambiguous signals over a larger portion of swath in the y-direction.

A. Observation Geometry

The geometry of observation is related to the transmit and receive positions as well as the related surface specular point (see Fig. 3). From the local incidence angle (θ) and the altitudes (H_t and H_r) of satellites, we can compute the range of satellites to the center of the imaging area (see Fig. 3). For simplicity, we assume a spherical earth to illustrate the concept without loss of generality. The equations linking the ranges and angles for transmit are

$$R_{0t}\sin\theta = (H_t + R_E)\sin\xi_t \tag{1}$$

$$R_{0t}\sin\theta_{lt} = R_E \sin\xi_t. \tag{2}$$

Then

$$\theta_{lt} = \sin^{-1}\left(\frac{R_E}{H_t + R_E}\sin\theta\right). \tag{3}$$

We can compute ξ_t using the following equation:

$$\xi_r = \theta - \theta_{lr}. \tag{4}$$

Therefore, the range from the transmit satellite to the center of imaging area is

$$R_{0t} = (H_t + R_E)\frac{\sin\xi_t}{\sin\theta}. \tag{5}$$

Similarly, for the receiving geometry

$$\theta_{lr} = \sin^{-1}\left(\frac{R_E}{H_r + R_E}\sin\theta\right) \tag{6}$$

$$\xi_r = \theta - \theta_{lr} \tag{7}$$

$$R_{0r} = (H_r + R_E)\frac{\sin\xi_r}{\sin\theta}. \tag{8}$$

For simplicity, we will assume that the transmit satellite is stationary; this is a reasonable approximation for the MUOS satellites at the geosynchronous altitude, which move slowly over time. Hereafter, we will focus on the motion of receiving satellites for SAR image formation in the rest of this article.

Each SoOpSAR satellite has two antennas with one (earth-viewing) pointing toward the land surfaces for recording reflected signals and the other one toward the MUOS satellite to record a copy of the transmit signal for subsequent match filtering processing (see Figs. 1 and 3). The antenna for the transmit signal from MUOS will be denoted as the "direct" antenna.

B. Modeling of Reflected Signals

Let us represent the transmit signal by

$$E_T(t) = \sqrt{P_T}\,a(t)\,e^{i2\pi f_c t} \tag{9}$$

where $a(t)$ is a narrow band signal, f_c is the center frequency, and P_T is the transmit power.

The reflected signal received by the earth-viewing antenna of the mth satellite receiver can be a straightforward generalization of the expression indicated in [24]

$$E_{rm}(t) = \int g(\bar{r})\,\gamma(\bar{r})\,a\left(t - \frac{r_{1m} + r_2}{c}\right)$$
$$\times \frac{e^{-ik(r_{1m}+r_2)}}{r_{1m}r_2}e^{i2\pi f_c t}d\bar{r} \tag{10}$$

where the wavenumber is $k = \frac{2\pi}{\lambda}$ and λ is the wavelength at the center frequency (f_c). $\gamma(\bar{r})$ accounts for the bistatic surface scattering.

For the Kirchhoff approximation (KA) of surface scattering [37], [38]

$$\gamma = F_{\beta\alpha} \tag{11}$$

where γ is related to the Fresnel reflection coefficient for incident polarization "α" and scattering polarization "β." The scattering coefficient $F_{\beta\alpha}$ is given in Appendix A.

The shape of transmit signal is denoted by $a(t)$ with a unity power. For a transmit signal with a bandwidth of B, the power density of a is $1/B$. r_{1m} and r_2 are the distance from $\bar{r}$ to the receive and transmit satellites, respectively. Then, $g(\bar{r})$ accounts for the antenna patterns of transmitter and receiver, G_T and G_R, respectively, as well as the transmit power

$$g(\bar{r}) = i\frac{\sqrt{P_T G_T(\bar{r})G_R(\bar{r})}}{4\pi}. \tag{12}$$

The distance from the mth receiver to $\bar{r}$ can be expressed as

$$r_{1m} = |\bar{r}_{sm} - \bar{r}| \tag{13}$$

where $\bar{r}_{sm}$ is the position of the mth receiver at time t and is related to the velocity vector of satellite characterized by $\bar{v}_m$ and initial position ($\bar{r}_{sm0}$)

$$\bar{r}_{sm} = \bar{r}_{sm0} + \bar{v}_m t. \tag{14}$$

Let us further denote the relative position vector at $t = 0$ by

$$\bar{r}_{1m0} = \bar{r}_{sm0} - \bar{r} \tag{15}$$

and the relative distance by r_{1m0}. If $r_{1m0} \gg v_m t$, we have the approximation

$$r_{1m} \cong r_{1m0} + \hat{r}_{1m0} \cdot \bar{v}_m t. \tag{16}$$

Representing the Doppler shift by

$$f_{Dm} = -\frac{\hat{r}_{1m0} \cdot \bar{v}_m}{\lambda} \tag{17}$$

we can approximate the expression of received signals by

$$E_{rm}\,(t) = \int g\,(\bar{r})\,\gamma\,(\bar{r})\,a\left(t - \frac{r_{1m}+r_2}{c}\right)$$

$$\frac{e^{-ik(r_{1m0}+r_2)}}{r_{1m0}r_2}e^{i2\pi(f_c+f_{Dm})t}d\bar{r}. \tag{18}$$

For the receiver located in the middle of array (see Fig. 1), which is on the *x*–*z* plane, let us specify its location by

$$\bar{r}_{s0} = R_{0r}\,(-\sin\theta\hat{x} + \cos\theta\hat{z})\,. \tag{19}$$

Let the other receivers be displaced from the middle receiver with the initial position of the receiver indicated by

$$\bar{r}_{sm0} = \bar{r}_{s0}\, + \Delta\bar{r}_m. \tag{20}$$

The distance from the middle receiver to a point on the horizontal plane, $\bar{r} = x\hat{x} + y\hat{y}$, is

$$r_1 = |\bar{r}_{s0} - \bar{r}|\,. \tag{21}$$

Assuming $r_1 \gg |\Delta\bar{r}_m|$ and $|\bar{r}|$, we have

$$r_{1m0} \cong r_1 + \frac{\bar{r}_{s0}\cdot\Delta\bar{r}_m}{r_1}$$

$$+ \frac{1}{2r_1}\left[(\Delta\bar{r}_m)^2 - \left|\frac{\bar{r}_{s0}\cdot\Delta\bar{r}_m}{r_1}\right|^2\right] - \frac{\bar{r}\cdot\Delta\bar{r}_m}{r_1}. \tag{22}$$

Let

$$\phi_m = k\frac{\bar{r}_{s0}\cdot\Delta\bar{r}_m}{r_1} + \frac{k}{2r_1}\left[(\Delta\bar{r}_m)^2 - \left|\frac{\bar{r}_{s0}\cdot\Delta\bar{r}_m}{r_1}\right|^2\right]. \tag{23}$$

We obtain

$$E_{rm}\,(t) = e^{-i\phi_m}\,\int g\,(\bar{r})\,\gamma\,(\bar{r})\,a\left(t - \frac{r_{1m}+r_2}{c}\right)$$

$$\times\frac{e^{-ik(r_1+r_2)}}{r_1r_2}e^{i2\pi(f_c+f_{Dm})t}e^{ik\frac{\bar{r}\cdot\Delta\bar{r}_m}{r_1}}d\bar{r}. \tag{24}$$

The last term in the integral provides a change in phase due to the offset of the receiver position from the central plane and will allow a focusing using data from multiple receivers.

For simplicity, if all receivers are positioned on one line, i.e., $\Delta\,\bar{r}_m = y'_m\,\hat{y}'$, we obtain the following approximation by a Taylor series expansion to the second order:

$$r_{1m0} \cong r_1 + y'_m\sin\theta\sin\phi - \frac{y'_p y'_m}{R_{0r}}$$

$$+ \frac{y'^2_m}{R_{0r}}\left(1 - \sin^2\theta\sin^2\phi\right) \tag{25}$$

where

$$y'_p = y'\,\left(1 - \sin^2\theta\sin^2\phi\right) + x'\sin^2\theta\sin\phi\cos\phi. \tag{26}$$

Substituting the aforementioned equations into (24), we have

$$E_{rm}\,(t) = e^{-i\phi_m}\,\int g\,(\bar{r})\,\gamma\,(\bar{r})\,a\left(t - \frac{r_{1m}+r_2}{c}\right)$$

$$\times\frac{e^{-ik(r_1+r_2)}}{r_1r_2}e^{i2\pi(f_c+f_{Dm})t}e^{ik\frac{y'_p y'_m}{R_{0r}}}d\bar{r} \tag{27}$$

where

$$\phi_m = k\left[y'_m\sin\theta\sin\phi + \frac{y'^2_m}{R_{0r}}\left(1 - \sin^2\theta\sin^2\phi\right)\right] \tag{28}$$

This equation is a straightforward generalization of the signal model described in [24] with the addition of a phase term in the integral resulting from the displacement of the *m*th receiver off the incidence plane of the middle receiver. The phase term has a linear dependence on y', which will allow for the sparse array processing to sharpen the spatial resolution in the y' direction and can be used to reduce the level of ambiguities denoted in Figs. 1 and 2.

The motion of spacecraft introduces a Doppler shift in the reflected signal. For simplicity, let us assume that all receivers are moving in parallel with the same velocity vector along $\hat{x}'$ (see Fig. 1)

$$\bar{v}_m = v\,(\cos\xi_r\hat{x}' + \sin\xi_r\hat{z})\,. \tag{29}$$

Under the assumption that $R_{0r} \gg x$ and y, we have

$$f_{mD} \cong \frac{v}{\lambda}\left[\sin\theta\cos\xi_r\cos\phi + \frac{\cos\xi_r}{R_{0r}}x' - \cos\theta\sin\xi_r\right] \tag{30}$$

where

$$x' = x\cos\phi + y\sin\phi. \tag{31}$$

Note that the Doppler shift does not depend on the cross-track position (y') near the center of observation geometry. For a target located far away from the $x' - z'$ plane, there will be a quadratic dependence on y', and the iso-Doppler lines will be hyperbolic, rather than parallel to each other, as depicted in Fig. 1.

C. Match Filter Processing

The reflected signal can be recorded continuously and divided into short consecutive time segments (to be denoted as receiver gates) for data processing (see Fig. 4). The steps of receiver gates represent a slow time; for a short receive gate (T_w), the Doppler frequency change within the receiver gate can be considered negligible.

Let us perform a match filtering of the data collected during the *n*th receiver gate with focus on a point located at $\bar{r}_c = x_c\,\hat{x} +$
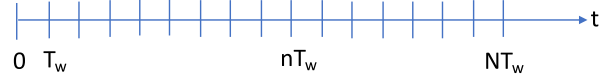

Fig. 4. Data divided into time windows of *N* receiver gates for processing. Each receiver gate can be considered as a slow time.

$y_c \hat{y}$

$$C_{nm} = \frac{1}{T_w} \int_{nT_w}^{(n+1)T_w} a\left(t - \frac{r_{1mc} + r_{2c}}{c}\right)$$

$$e^{ik(r_{1m0c}+r_{2c})} e^{-i2\pi(f_c + f_{Dm}(\bar{r}_c))t} E_{rm}(t)\, dt. \qquad (32)$$

Here, we assume that the transmit waveform can be derived from the direct signal with negligible noise. The impact of noisy transmit waveform will be addressed later in Section IV in terms of interferometric processing loss (IPL).

Substituting (27) into the aforementioned equation, we obtain

$$C_{nm} = \int d\bar{r}\, g(\bar{r}) \gamma(\bar{r}) \frac{e^{-ik[(r_{1m0}+r_2)-(r_{1m0c}+r_{2c})]}}{r_{1m0} r_2}$$

$$\frac{1}{T_w} \int_{nT_w}^{(n+1)T_w} a\left(t - \frac{R}{c}\right) a\left(t - \frac{R_c}{c}\right) e^{i2\pi \Delta f_{Dm} t}\, dt \qquad (33)$$

where

$$R = r_{1m} + r_2 \qquad (34)$$

and

$$R_c = r_{1mc} + r_{2c} \qquad (35)$$

r_{1m0c} and r_{2c} are r_{1m0} and r_2 evaluated at $\bar{r}_c = \bar{r}$, respectively. For the Doppler shift, we have

$$\Delta f_{Dm} = f_{Dm}(\bar{r}) - f_{Dm}(\bar{r}_c). \qquad (36)$$

If the Doppler shift within one receiver gate (T_w) is negligible, $1 \gg T_w \Delta f_{Dm}$, we can pull the Doppler-related part out of the time integral with $t = nT_w$ to allow the isolation of range compression

$$C_{nm} \cong \int d\bar{r}\, g(\bar{r}) \gamma(\bar{r}) \frac{e^{-ik[(r_{1m0}+r_2)-(r_{1m0c}+r_{2c})]}}{r_{1m0} r_2}$$

$$e^{i2\pi \Delta f_{Dm} n T_w} R_{nmp} \qquad (37)$$

where the range compression term is expressed as

$$R_{nmp} = \frac{1}{T_w} \int_{nT_w}^{(n+1)T_w} a\left(t - \frac{R}{c}\right) a\left(t - \frac{R_c}{c}\right)\, dt. \qquad (38)$$

Assuming $R_{0r} \gg x, y, x_c, y_c$, we obtain

$$C_{nm} = \int d\bar{r}\, g(\bar{r}) \gamma(\bar{r}) \frac{e^{-ik[(r_1+r_2)-(r_{1c}+r_{2c})]}}{r_1 r_2}$$

$$e^{ik\left(\frac{y'_p - y'_{pc}}{R_{0r}}\right) y'_m} e^{i2\pi \Delta f_{Dm} n T_w} R_{nmp}. \qquad (39)$$

The complete match filtering processing includes two additional summations to account for the Doppler filtering and sparse array processing

$$S(x_c, y_c) = \frac{1}{M_t N_r} \sum_m \sum_n A_m C_{nm}. \qquad (40)$$

M_t and N_r are the total number of terms for averaging. The summation over n is for Doppler filtering, whereas the summation over m is for the sparse receiver array processing. The weighting factor A_m can be adjusted to weight the signal from each receiver to tradeoff resolution and sidelobe levels

$$S(x_c, y_c) = \int d\bar{r}\, g(\bar{r}) \gamma(\bar{r}) \frac{e^{-ik[(r_1+r_2)-(r_{1c}+r_{2c})]}}{r_1 r_2} P_{\mathrm{TR}}. \qquad (41)$$

In the aforementioned equation, P_{TR} can be identified as the point target response

$$P_{\mathrm{TR}} = \frac{1}{M_t N_t} \sum_m \sum_n A_m e^{ik\left(\frac{y'_p - y'_{pc}}{R_{0r}}\right) y'_m}$$

$$\times e^{i2\pi \Delta f_{Dm}(\bar{r},\bar{r}_c) n T_w} R_{nmp} \qquad (42)$$

where the Doppler shift is

$$\Delta f_{Dm} = \frac{v \cos \xi_r}{\lambda} \left(\frac{x' - x'_c}{R_{0r}}\right). \qquad (43)$$

1) Range Compression: Expressing the integral using the frequency spectrum of $a(t)$, we have

$$R_{nmp} = \frac{1}{2\pi} \int |A(\omega)|^2 e^{-i\omega \frac{R - R_c}{c}}\, d\omega. \qquad (44)$$

Let us assume that the transmit signal waveform has a bandwidth of B and a flat power spectrum with $|A|^2 = \frac{1}{B}$; therefore, the response function for range compression is

$$R_{nmp} = \operatorname{sinc}\left(B \frac{R - R_c}{c}\right). \qquad (45)$$

Here, $\operatorname{sinc}(x) = \frac{\sin(\pi x)}{\pi x}$.

For $R_{0r} \gg x, y, x_c, y_c, vt$, we can obtain the following approximation:

$$R - R_c \cong -\frac{v \cos \xi_r n T_w}{R_{0r}} (x' - x'_c) - \frac{(y'_p - y'_{pc}) y'_m}{R_{0r}}$$

$$+ \frac{1}{2}\left(\frac{R_{0r} + R_{0t}}{R_{0r} R_{0t}}\right)\left[(x^2 - x_c^2)\cos^2\theta + (y^2 - y_c^2)\right]. \qquad (46)$$

The first term is due to the motion of receivers. The second term due to the offset of receiver position will introduce a phase offset off the focus. "y'_{pc}" is "y'_p" are evaluated at the location of focusing. The third term will produce a range compression response with equal value on iso-range contours, depicted as concentric ellipses in Fig. 1.

2) Near Focus Approximation for P_{TR}: If (x,y) is near the focal point (x_c, y_c), the first two terms can be neglected, and hence, R_{nmp} does not depend on n and m

$$R_{nmp} = R_p. \qquad (47)$$

Note that the Doppler filtering will focus the energy mostly near $x = x_c$; therefore, the neglection of the first term will nominally introduce relatively small errors after the Doppler filtering. Should the sparse array be applicable to reduce the energy near the ambiguity, then the neglection of the second term can also be justified.

The point target response of the SoOpSAR with an array of receivers can then be approximated by the product of three terms:

range compression (R_p), Doppler filtering (D_p), and array factor (A_p) of the sparse array

$$P_{\text{TR}} = R_p \, D_p A_p. \tag{48}$$

We can carry out the integration or summation of each term separately. The Doppler filtering can be expressed as

$$D_p = \frac{1}{2N+1} \sum_{n=-N}^{N} e^{i2\pi[f_{Dm}(\bar{r}) - f_{Dm}(\bar{r}_c)]nT_w}. \tag{49}$$

We then have

$$D_p = \frac{1}{2N+1} \frac{\sin\left(\pi\,(2N+1)\,T_w\Delta f\right)}{\sin\left(\pi T_w\Delta f\right)} \tag{50}$$

with the total integration time $T = (2N+1)T_w$.

If $T_w\Delta f \ll 1$, the summation can be approximated by an integral with an integration time of T

$$D_p(x) \cong \frac{1}{T} \int_{-\frac{T}{2}}^{\frac{T}{2}} e^{i2\pi f_D t} e^{-i2\pi f_{Dc}t} dt$$

$$= \text{sinc}\left[T \frac{v \cos\xi_r \, (x' - x'_c)}{\lambda \quad R_{0r}} \right]. \tag{51}$$

We can also introduce the normalized array response function

$$A_p = \frac{1}{M_t} \sum_{m=-M}^{M} A_m e^{ik \frac{y'_m}{R_{0r}} (y'_p - y'_{pc})} \tag{52}$$

$$M_t = \sum_{m=-M}^{M} A_m. \tag{53}$$

For a uniform weighting and spacing, i.e., $A_m = 1$ and $y'_m = m\Delta$, the array factor will be

$$A_p = \frac{\sin\left((2M+1)\,\beta\right)}{(2M+1)\sin\beta} \tag{54}$$

where

$$\beta = \frac{\pi\Delta}{\lambda R_{0r}} \, (y'_p - y'_{pc}). \tag{55}$$

For a relatively long integration time, the spatial resolution of the point target response along track (x) is primarily controlled by the Doppler filtering based on (51)

$$\delta x \cong \frac{\lambda R_{0r}}{Tv\cos\xi_r}. \tag{56}$$

The across-track resolution (δy) is determined by a combination of range compression and focusing of the sparse array factor. From (45), the slant range resolution due to the range compression is

$$\Lambda = \frac{C}{B}. \tag{57}$$

The associated across-track resolution due to range compression is then determined by the third term in (46). When the point of interest is close to the center of swath (i.e., $y_c \sim 0$), the across-track resolution (δy) due to range compression is

$$\delta y = 2\sqrt{\frac{2\Lambda R_{0r}R_{0t}}{R_{0r} + R_{0t}}}. \tag{58}$$

If the point of focus is far away from the central plane, then it can be derived from the third term in (46) by letting $y \approx y_c$ and $\delta y = y - y_c$

$$\delta y \cong \frac{\Lambda R_{0r} R_{0t}}{y_c \, (R_{0r} + R_{0t})}. \tag{59}$$

This indicates that the spatial resolution resulting from the range compression will improve as the focal point (y_c) moves further off the *x*-axis.

The focusing effect of the sparse array of receivers is approximately proportional to the total width of the array, $D_a = (2M+1)\Delta$, based on (54)

$$\delta y \cong \frac{\lambda R_{0r}}{D_a}. \tag{60}$$

We find that the across-track resolution is limited either by the range compression, (58) or (59), or by the antenna array factor, (60).

III. DOPPLER BANDWIDTH AND INTEGRATION TIME

The maximum coverage area is determined by the width of receiver gate T_w. From the iso-range equation, the width of the illuminated area across track is

$$W_y = 2\sqrt{2cT_w \frac{R_{0t}R_{0r}}{R_{0t} + R_{0r}}} \tag{61}$$

and the along-track width is

$$W_x = \frac{W_y}{\cos\theta}. \tag{62}$$

Fig. 5 shows that the width (W_y) can reach 500 km for a receiver gate width of 0.1 ms based on the parameter values indicated in Table I. It can also be seen that the dimension of coverage along flight direction (*x*) can be several hundreds of kilometers. Given the ground track speed of LEO satellites (V_g), about 7 km/s, the large along-track coverage allows a long dwell time. The nominal ground track velocity is about 6.7 km/s for a LEO satellite, and hence, the allowable dwell time, $\sim W_x$ divided by V_g, will be >10 s, for points within the area covered by one receiver gate.

The Doppler bandwidth of the reflected signal within the coverage area is

$$f_{\text{DB}} = \frac{v}{\lambda} \frac{W_x \cos\phi}{R_{0r}} \cos\xi_r. \tag{63}$$

Fig. 6 indicates an increase of the Doppler bandwidth versus receiver gate width, and a decrease of the sampling frequency ($1/T_w$). To resolve the Doppler shift, a nominal criterion is to choose the sampling frequency to be at least 2.3 times of the Doppler bandwidth

$$\frac{1}{T_w} > 2.3 f_{\text{DB}}. \tag{64}$$

From the intercept of black- and red-dashed lines, it can be determined that the receiver gate width should be 0.1 ms or shorter in order to meet this criterion.
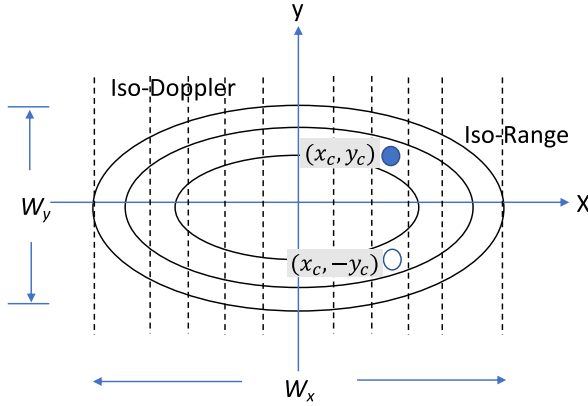
Fig. 5.   Left panel: Area of coverage for the signals detected during each receiver gate. Dashed lines indicated iso-Doppler lines and solid ellipses indicate iso-range contours. The dimension of the outermost ellipse depends on the width of receiver gate (T_w). Right panel: along-track (W_x) and swath width (W_y) dependence on T_w.

TABLE I
KEY DESIGN PARAMETERS

Parameters	Characteristics
MUOS altitude, H_t	35,786 km
MUOS EIRP or ($P_t G_t$)	43 dBW
SoOpSAR Receiver altitude, H_r	675 km
Number of receivers	3 to 13
Receiver spacing, Δ	100 m
Center Frequency	360 MHz
Bandwidth (B)	20 MHz
Integration time (T)	Up to ~10 seconds
Antenna gain (G_r) for the Earth-viewing antenna	15 dBi
Half power beamwidth of the Earth-viewing antenna	25 degrees
Receiver noise temperature (T_{sys}) for reflected signals	290 K
Peak antenna gain of the direct antenna	6 dBi
Half-power beamwidth of the direct antenna (deg)	60 degrees
Receiver noise temperature for direct signal	100 K
Interferometric processing loss	3 dB

Note: IPL is due to the use of direct signal for range compression.

However, we need to be cautious that the iso-range equation defined by an ellipse is only accurate if the dimension of ellipse is much smaller than R_{0r} and R_{0t}; this is the assumption for the derivation of the quadratic phase term in (46). We can choose a smaller range gate of 0.01 ms, the width of illuminated area in y remains quite large, around 200 km indicated by Fig. 5.

IV. PERFORMANCE ANALYSIS

A. Spatial Resolution

The spatial resolution of SoOpSAR is defined by the Doppler filtering, range compression, and the array of receivers, not
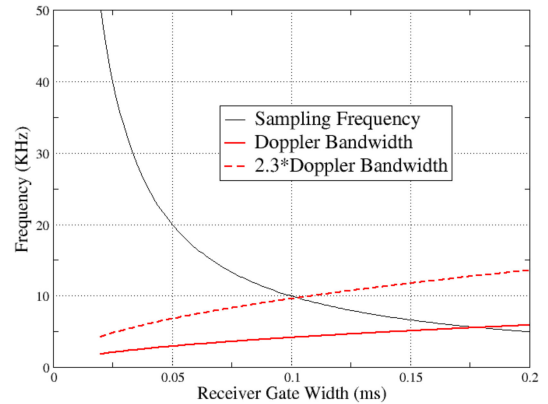

Fig. 6.   Doppler bandwidth of the reflected signals detected within the receiver gate. Doppler bandwidth (red solid curve); 2.3 times of Doppler bandwidth (red dashed line); and sampling frequency, $1/T_w$ (black). The curves for sampling frequency and 2.3 times of Doppler bandwidth cross over at the receive gate width of about 0.1 ms.

by the radius of Fresnel zones, nor by the surface scattering processes. The SoOpSAR uses the nominal definition of spatial resolution for radar remote sensing with the region enclosed by the 3-dB contour.

Here, we use the parameters outlined in Table I to illustrate the potential performance of SoOpSAR. The angle of incidence (θ) at the center of imaging area is 45°. The receivers are assumed to be moving on the x–z and parallel planes with a flight velocity of 6.7 km/s.

The SoOpSAR concept can be visualized by illustrating the results of each step of data processing. The range compression (R_{nmp}) with $n = 0$ and $m = 0$ of the reflected signal from a point located at $(x_c, y_c) = (0$ km, 15 km$)$ produces an elevated elliptical ring (left panel of Fig. 7), corresponding to an iso-range contour (see Fig. 1). Applying the additional Doppler filtering (D_p) reduces the response off the plane defined by $x = x_c$ (middle panel of Fig. 7), resulting in two major ambiguous sharp peaks. One of the sharp peaks corresponds to the target position, whereas the other peak is the iso-range ambiguity located at $y = -y_c$. These two peaks with the same Doppler frequency
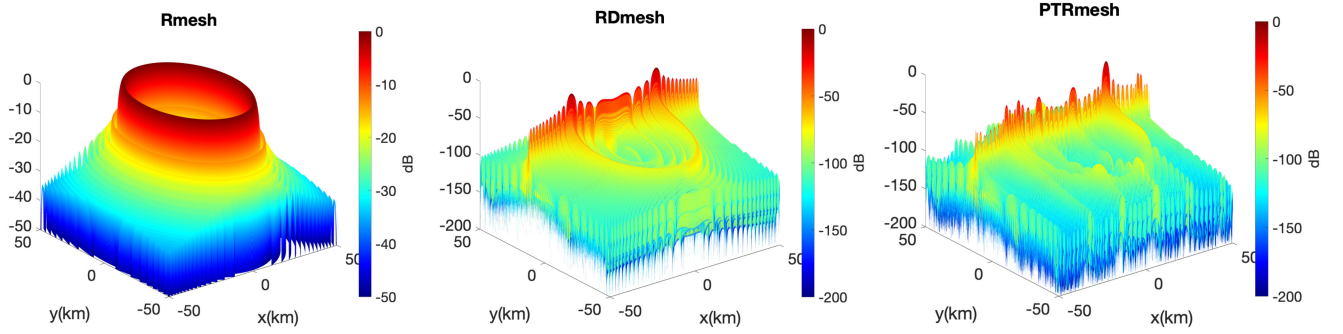
Fig. 7. Point target response with an array of seven receivers for a target located at $x_c = 0$ km and $y_c = 10$ km: range compression only (left), after Doppler filtering and range compression (middle), and including sparse array (right). The receiver spacing is 100 m and an integration time of 2 s is used for Doppler filtering.
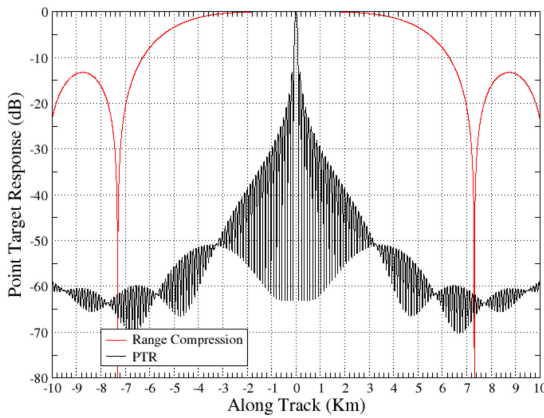

Fig. 8. Point target response, range compression, sparse array, and full array factor along track at $y_c = 15$ km. The integration time is 0.5 s, rather than 2 s, so that individual sidelobes can be distinguished in the chart.

and delay cannot be separated in delay and Doppler. The right panel of Fig. 7 indicates that the array factor can reduce the level of range ambiguity (mirrored with respect to the plane of flight).

The along-track response after range compression and Doppler filtering is illustrated in Fig. 8. The spatial resolution achievable from the range compression is about 11 km (3-dB threshold in the red curve). The Doppler filtering with an integration time of $T = 2$ s allows the sharpening of spatial resolution to about 50 m in 3 dB from the peak. As discussed earlier, the dwell time can reach a few to 10 s. Therefore, a longer integration time of 10 s can be used to improve the along-track resolution to 10 m.

The across-track response for an array of five receivers is illustrated for three cases (see Fig. 9). For the target located in the middle of swath ($y_c = 0$ km), the width of range compression produces a 3-dB width of about 10 km. The resolution of P_{TR} in this case is determined by the array factor (upper panel). For a target located at $y_c = 10$ km, the array factor and range compression have comparable impact on resolution (middle panel). In this case, the amplitude of range ambiguity at $y_c = -10$ km reduces to about –20 dB by the array factor. For a target further off the central plane at $y_c = 25$ km (lower panel),

the resolution of P_{TR} is essentially determined by the range compression. We find that the combined effects of the array factor and range compression can improve the spatial resolution and reduce the ambiguity level.

However, there are locations where the ambiguity level at $y = -y_c$ cannot be reduced. Due to the nature of a sparse array with the spacing between elements to be much greater than one wavelength, there are many aliases in the array factor (black curves in Fig. 9). The spacing between the adjacent aliases in the sparse array pattern is

$$\delta_a \cong \frac{\lambda R_{0r}}{\Delta}. \tag{65}$$

Given the spacing of $\Delta = 100$ m and the values of other parameters used for the illustration in Fig. 9, the spacing of adjacent aliases is about 7.2 km. When the location of range ambiguity and one of the aliases coincide, the ambiguity level cannot be reduced by the array factor

$$- y_c = y_c - m\delta_a \tag{66}$$

where m is an integer. Therefore, the specific locations are given by

$$y_c = \frac{m\delta_a}{2}. \tag{67}$$

Fig. 10 provides an example of the point target response for a target located at $y_c = 15$ km, which is very close to a multiple of $\delta_a = 3.6$ km. In this case, one of the array factor aliases is very close to the location of the mirrored iso-range ambiguity with the peaks of black and red curves close together.

Based on the point target response, we can evaluate the level of the "mirrored" ambiguity level ($y = -y_c$) for a given point target located at y_c. An integration of $|P_{\mathrm{TR}}|^2$ was carried out over $\pm$ four times of the spatial resolution at the focal point and the mirrored location. The ratio was taken and defined as the ambiguity to signal ratio (ASR). We find that the ASR level for many ambiguities can still be low. The ASR levels will reduce with the number of receivers (see Fig. 11). With more than five receivers, a major portion of the swath can have an ASR value of lower than 0.05. Table II shows the percentage of swath that can reach below such a threshold for two different receiver spacings and two different ASR thresholds.

Fig. 10. Point target response across track at $x = 0$ km for a point target located at $x_c = 0$ and $y_c = 15$ km. The spacing between receivers is 100 m.
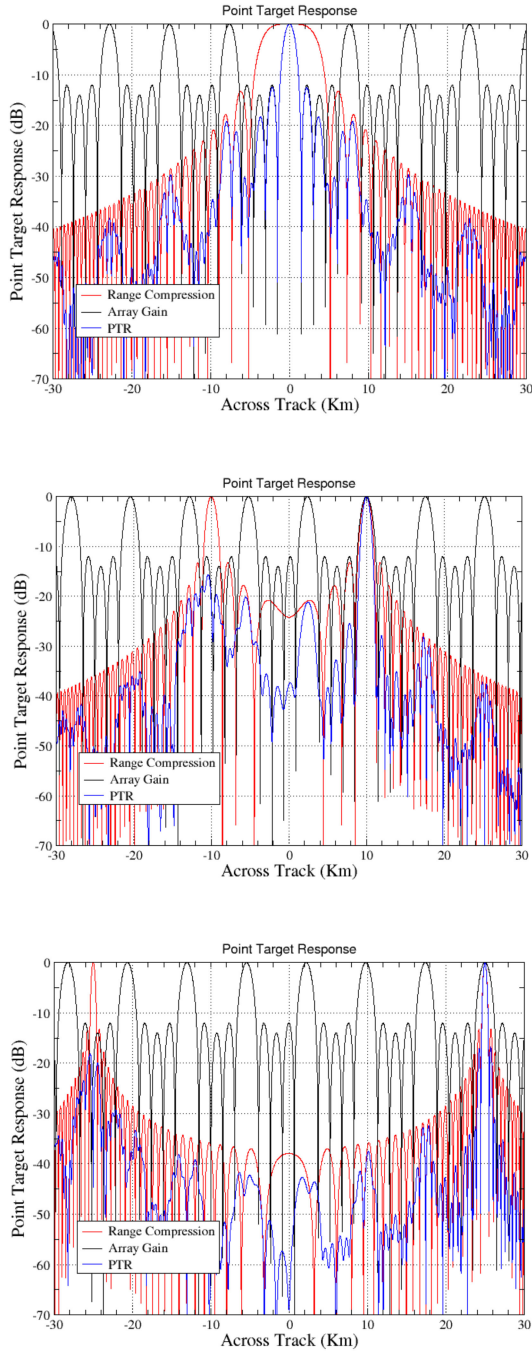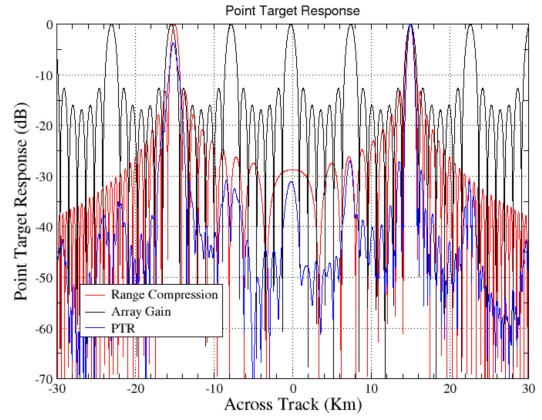

Fig. 9. Point target response for an array of five receivers across track at $x = 0$ km for a point target located at $x_c = 0$ and $y_c = 0$ km (upper panel), $y_c = 10$ km (middle panel), and $y_c = 25$ km (lower panel). The spacing between adjacent receivers is 100 m.
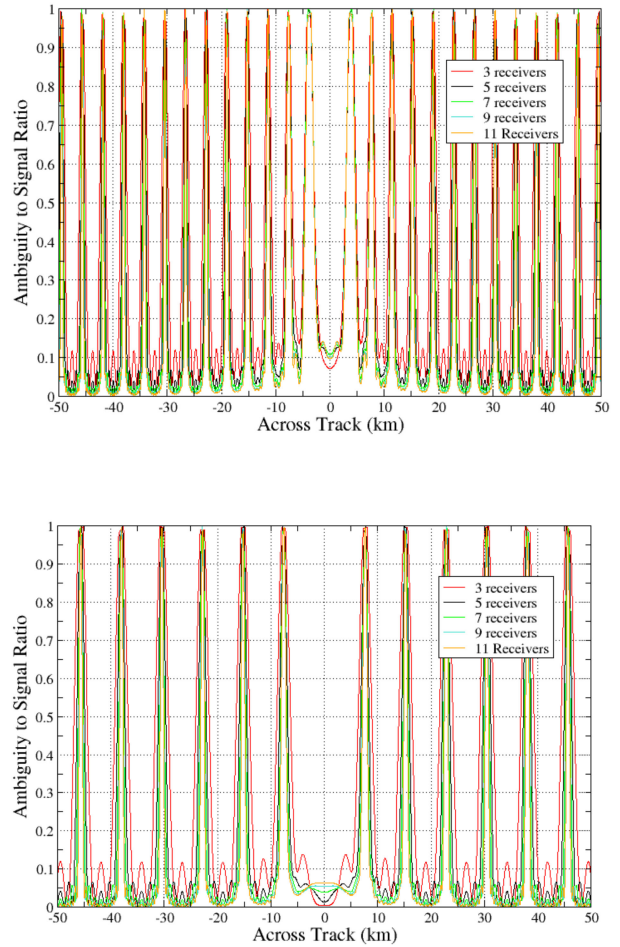
Fig. 11. ASR versus the location of a point target. (Top) the spacing between receivers is 100 m. (Bottom) the spacing is reduced to 50 m, resulting a doubling in spacing between aliases.

As the number of receivers increases, the portion of swath with ASR < 0.05 (or 0.1) increases. It is found that a smaller spacing between receivers is better for a reduced ambiguity level, but the spatial resolution in the central portion of swath will degrade, as indicated by (60). An ambiguity ratio level of < 0.05 for about 70% of the swath is achievable with seven receivers and $\Delta = 50$ m, and the percentage can reach 87% for ASR < 0.1.

The spatial resolution, defined as the half-power width of the P_{TR}, with respect to the number of receivers is illustrated in

Fig. 12. The along-track resolution for an integration time of 2 s is about 50 m (orange dashes). A longer integration time of 10 s will reduce it to 10 m. The across-track resolution near the central portion of swath depends on the number of receivers, i.e., the total aperture width of receiving antennas (D_a), and can

TABLE II
PERCENTAGE OF SWATH WITH AN ASR VALUE OF LOWER THAN 0.05 OR 0.1

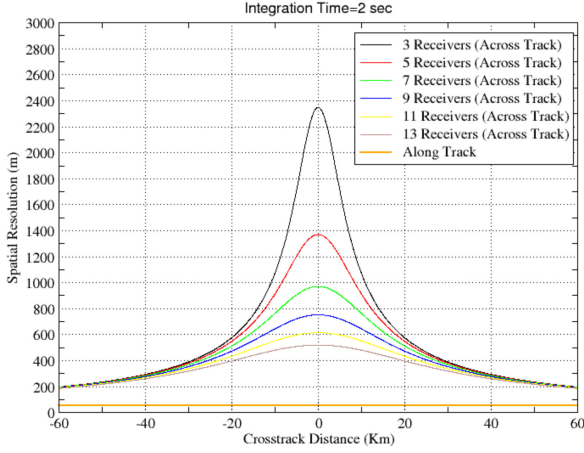| # of receivers	Percentage of swath for Δ=50m		Percentage of swath for Δ=100m	
	ASR<0.05	ASR<0.1	ASR<0.05	ASR<0.1
3	26	43	16	36
5	53	78	40	65
7	72	87	55	73
9	75	91	63	78
11	79	94	67	82

Fig. 12. Spatial resolution of a point target versus cross-track distance. The spacing of receivers is 100 m and integration time is 2 s. The along-track resolution is about 50 m (orange dashes).

reach 500 m with 13 receivers and 1 km with 7 receivers. The across-track resolution improves with an increasing cross-track distance. At the far swath, it is dictated by the range compression, reaching about 200 m at 50 km off the center of swath. Based on (59), the resolution can reach 100 m at 100 km off the center of swath, not shown in the figure.

B. Signal-to-Noise Ratio

The formulation and expressions of SNR for reflectometry have been established by Alonso-Arroyo *et al.* [40] and Martin-Neira [41]. To evaluate the power level of reflected signals, it requires knowledge on the amplitude of surface scattering signals, which consist of two components. The first term corresponds to the coherent reflection from an infinite planar surface, [40, (21)], whereas the second term corresponds to the diffused scattering, [40, (22)]. For the coherent term, the propagation loss can be described by a mirror reflection of a spherical wave with a quadratic dependence on the total distance

$$\frac{1}{(R_{0t} + R_{0r})^2}.$$

For the incoherent term, the total propagation loss is the product of propagation losses of incidence and scattering waves

$$\frac{1}{(R_{0t} R_{0r})^2}.$$

For SoOpSAR, the second term due to the incoherent (diffused) scattering remains applicable, but the expression of the coherent contribution will differ because the spatial integration will be carried out only over the area with a significant value in P_{TR}, not over an infinite planar surface.

We can derive the coherent and incoherent scattering power for SoOpSAR based on the matchup filter output (41). The diffused scattering by rough surfaces will be modeled by the KA [37], [38]. The surface height is characterized by $z = f(x, y)$. The position vector of a point on the surface then becomes $\bar{r} = x\hat{x} + y\hat{y} + f(x, y)\hat{z}$. Applying the Taylor series expansion to the distances from satellites to the point of scattering, we obtain the extra phase change of the reflected signal due to the surface elevation

$$e^{i\psi} = e^{ik\beta f(x,y)} \tag{68}$$

where

$$\beta = \frac{R_{0t}}{r_2} \cos\theta_i + \frac{R_{0r}}{r_1} \cos\theta_s. \tag{69}$$

The match filter output including the rough surface effects can be an extension of (41) and expressed as

$$S(x_c, y_c) = \int d\bar{r}\, g(\bar{r})\, \gamma(\bar{r}) \frac{e^{-ik[(r_1+r_2)-(r_{1c}+r_{2c})]}}{r_1 r_2} P_{TR} e^{i\psi}. \tag{70}$$

By assuming a Gaussian probability density with a standard derivation of σ_h for the surface roughness function f, the expected value of the phase term is

$$< e^{i\psi} > = e^{-\frac{1}{2}k^2\beta^2\sigma_h^2}. \tag{71}$$

Here, the ensemble average is denoted by the angular brackets.

The coherent part of signals scattered by the rough surface is the expected value of the match filter output

$$\langle S(x_c, y_c) \rangle = \int d\bar{r}\, g(\bar{r})\, \gamma(\bar{r}) \frac{e^{-ik[(r_1+r_2)-(r_{1c}+r_{2c})]}}{r_1 r_2} P_{TR} \langle e^{i\psi} \rangle. \tag{72}$$

Assuming that the surface reflection coefficient, characteristics of surface roughness, and antenna gain are constant near the focal point where the value of P_{TR} is significant, we can express the power of the coherent term as

$$P_{Sc} = |\langle S(x_c, y_c) \rangle|^2 = \frac{P_T G_T(\bar{r}_c)\, G_R(\bar{r}_c)\, \gamma_{coh}^2}{(4\pi)^2 (R_{0t} R_{0r})^2} (A_{\text{eff}})^2 |F_w|^2 \tag{73}$$

where the effective area accounts for the shape of P_{TR}

$$A_{\text{eff}} = \int d\bar{r}\, |P_{TR}|^2 \tag{74}$$

and F_w accounts for the phase variation over the region of integration, primarily limited by the value of P_{TR}

$$F_w = \frac{1}{A_{\text{eff}}} \int d\bar{r} P_{TR} e^{-ik[(r_1+r_2)-(r_{1c}+r_{2c})]}. \tag{75}$$

Note that the phase of the second term in the aforementioned integral will vary over Fresnel zones. If the phase variation over the region that can be resolved by P_{TR} is over 2π, the value of F_w will be diminished. The more Fresnel zones that can fit into the region of integration limited by P_{TR}, the smaller is F_w.

However, if the spatial resolution or region of integration is much larger than the size of Fresnel zone, i.e., $P_{\text{TR}} \approx 1$, F_w is the Fresnel integral and can be integrated out by the stationary phase method. In this case, the expression of coherent power corresponds to the coherent reflection by an infinite planar surface, indicated in [40]

$$P_{Sc} \cong \frac{P_T G_T\left(\bar{r}_c\right) G_R\left(\bar{r}_c\right)\left(\frac{\gamma_{coh}}{\cos\theta}\right)^2}{4\pi\left(R_{0t}+R_{0r}\right)^2}\frac{\lambda^2}{4\pi}. \tag{76}$$

For the target location close to the specular point such that $\theta_i \approx \theta_s$ and, hence, $\beta = 2\cos\theta_i$, the reflection term can be expressed as

$$\gamma_{coh}^2 = |F_{\beta\alpha}|^2\, e^{-4k^2\sigma_h^2\cos^2\theta_i}. \tag{77}$$

For the incoherent part of scattered signals, the power of the random component of $S(x_c, y_c)$ caused by rough surface scattering is

$$P_{Si} = \left\langle \left| S\left(x_c, y_c\right) - \left\langle S\left(x_c, y_c\right)\right\rangle \right|^2 \right\rangle. \tag{78}$$

We follow the same approach as described in [37] and [38] to derive the power of the diffused scattering term under the assumption that the correlation length of surface roughness, $f(x, y)$, is much smaller than the spatial dimension of footprint, characterized by P_{TR}. This leads to the following nominal expression for the incoherent normalized radar cross section (σ_0) of rough surfaces and the expression of incoherent power

$$P_{Si} = \frac{P_T G_T\left(\bar{r}_c\right) G_R\left(\bar{r}_c\right)\sigma_0}{(4\pi)^2\left(R_{0t} R_{0r}\right)^2}\frac{\lambda^2 A_{\text{eff}}}{4\pi}. \tag{79}$$

This is the radar equation of SAR signals described in [39], which neglects the coherent signals.

The total power of the match filter output is the sum of the coherent and incoherent terms described by (73) and (79)

$$P_S = P_{SC} + P_{Si}. \tag{80}$$

For the power of noise after match filtering, the results from Krieger and Moreira [39] are applicable. The power of noise after range compression, Doppler filtering, and accounting for additional coherent averaging effect of the sparse array factor after some algebraic manipulation can be expressed as

$$P_N = \frac{k_B}{M_t^2 N_r T_w}\sum_m |A_m|^2 T_{rm} \tag{81}$$

where k_B is the Boltzmann constant and T_{rm} is the noise temperature of the mth receiver. If $A_m = 1$ and all receivers have the same noise temperature T_r, we have

$$P_N = \frac{k_B T_r}{M_t N_r T_w}. \tag{82}$$

From these equations, we can compute

$$\text{SNR}_c = \frac{P_S}{P_N} \tag{83}$$

which would be the SNR if the transmit waveform is perfectly known and used for match filtering.

C. Leakage Into Antenna Sidelobe

The transmit signal from MUOS can enter the direct antenna, but also the sidelobe of the earth-viewing antenna. They can be described as for the direct signal into the mth satellite

$$E_{dm}\left(t\right) = i\frac{\sqrt{P_T G_T\left(\bar{r}_d\right) G_{Rdm}\left(\bar{r}_d\right)}}{4\pi R_d}\lambda a$$
$$\times \left(t - \frac{R_d}{c}\right)e^{-ikR_d}e^{i2\pi(f_c+f'_{dm})t} \tag{84}$$

and for the sidelobe leakage into the earth-viewing antenna

$$E_{drm}\left(t\right) = E_{dm}\left(t\right)\sqrt{\frac{G_{Rdrm}}{G_{Rdm}}} \tag{85}$$

where G_{Rdm} and G_{Rdrm} are the antenna gains of the direct and earth-viewing antennas, respectively.

Including E_{drm} as part of the received signal and carrying out the match filtering process, we can show that the expected power of the sidelobe leakage can be approximated by

$$P_{dr} = \frac{P_T G_T\left(\bar{r}_d\right) G_{Rdr}\left(\bar{r}_d\right)}{\left(4\pi R_d\right)^2}\lambda^2 R_{nmp}^2\left(B\frac{R_{0t}+R_{0r}-R_d}{c}\right). \tag{86}$$

Note that R_{nmp} is the range compression function described by (45).

The power of the sidelobe leakage into the earth-viewing antenna can be strong, but the leakage signal arrives much earlier than the reflected signal and, hence, its power will be reduced by the range compression function, the last term in (86), which is the cross-correlation with the transmit waveform. Using the parameters indicated in Table I for a footprint located at an incidence angle of 45°, the difference in time delay between the direct and reflected signals is about 3 ms, leading to a range compression loss of –105 dB. In addition, the direct signal enters the sidelobe of the earth-viewing antenna at 88.6° from the boresight, where the antenna gain is expected to be much lower than 0 dBi. An evaluation of (86) shows that the power level of P_{dr} is –247.5 dBW for an antenna sidelobe gain of –10 dBi. The expected noise power (P_N) is –215.4 dB for an integration time ($T = N_r\, T_w$) of 2 s, $M_t = 7$ and $T_{\text{sys}} = 290$ K based on (82). Therefore, the leakage power is expected to be about 30 dB below the noise floor and will have a negligible impact on the SNR of SoOpSAR. In addition, the leakage power can be calibrated (or subtracted) from the total signal power using the antenna gain ratio and range compression function based on (86).

D. Interferometric Processing Loss

Note that the transmit waveform of MUOS signal is generally unknown and has to be measured using the direct antenna. The IPL is due to the presence of noise in the direct signal for the estimation of transmit waveform [41]. Following the same formulation described in [41], we can show that the equation for the IPL shown in [41] is applicable to the SoOpSAR concept (see Appendix B). The SNR of the match filter output based on a noisy estimate of the transmit waveform is

$$\text{SNR} = \frac{\text{SNR}_c}{\text{IPL}} \tag{87}$$

and the IPL is expressed as

$$\text{IPL} = 1 + \frac{1 + \text{SNR}_r}{\text{SNR}_d} \tag{88}$$

where SNR_d is the SNR of the direct signal, whereas SNR_r is the SNR of the reflected signal. They can be computed by

$$\text{SNR}_d = \frac{P_d}{kT_{dN}B_d} \tag{89}$$

and

$$\text{SNR}_r = \frac{P_r}{kT_{rN}B_r} \tag{90}$$

where the receiver noise temperature is T_{dN} and T_{rN}, respectively, for direct and reflected channels. The power of direct signal can be expressed as

$$P_d = \frac{P_T G_T G_R}{4\pi R_d^2} \frac{\lambda^2}{4\pi} \tag{91}$$

whereas the power of reflected signals is characterized by the bistatic radar equation with integration over the earth surface

$$P_r = \int d\bar{r} \, \frac{P_T G_T\left(\bar{r}\right) G_R\left(\bar{r}\right) \sigma_0}{\left(4\pi\right)^2 \left(R_t R_r\right)^2} \frac{\lambda^2}{4\pi}. \tag{92}$$

There are many surface scattering models that can be used to estimate σ_0, including the KA.

There is a special case, useful to indicate as a reference, which is the isotropic scattering by rough surfaces with $\sigma_0/\cos\theta = 1$. Two additional approximations are made for this special case: namely the distance to transmitter is much greater than the distance to receiver and the MUOS transmitter antenna pattern does not vary over the region of illumination. They lead to the following expression for the power of scattered signals by the earth surface:

$$P_{\text{riso}} = P_T \, G_T \frac{\lambda^2}{\left(4\pi\right)^2 R_{0t}^2}. \tag{93}$$

This takes advantage of the following identity for integration of the directivity of earth-viewing antenna over all directions:

$$\int d\bar{r} \frac{G_R\left(r\right)}{R_r{}^2} \cos\theta = 4\pi. \tag{94}$$

We have evaluated SNR_r for a range of surface roughness conditions based on the soil dielectric constant model for the computation of Fresnel reflection coefficients [42]. Without loss of generality, we computed the bistatic normalized radar cross-section derived using a Gaussian spatial correlation function for the surface roughness with two parameters, correlation length (l_c), and rms height σ_h. The expressions of the bistatic normalized radar cross section in [37] are utilized.

SNR_r for several cases of rough surfaces are illustrated in Fig. 13. When the surface is relatively smooth with a small rms height ($\sigma_h < 2$ cm), SNR_r is –5 dB or lower. For very rough surfaces, SNR_r can be above 0 dB. Note that the integral for P_r is contributed by a very large region, about 2000 km in dimension defined by the receiver antenna beamwidth. The enclosed surfaces will be heterogeneous with various roughness
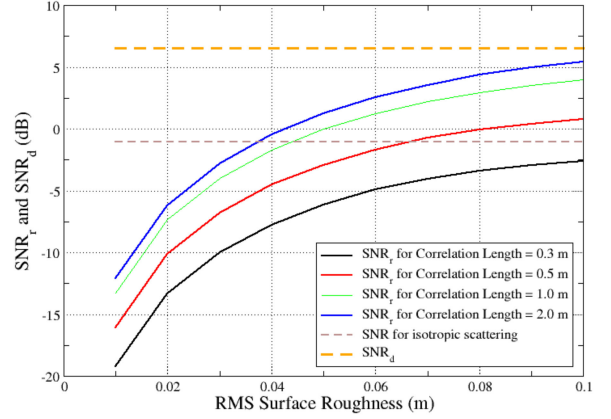

Fig. 13. SNRs of direct and reflected signals for a range of surface roughness under the KA for four correlation lengths. The SNR for isotropic scattering falls roughly in the middle of four cases under the KA. The SNR of direct signal is about 8 dB above the SNR of isotropic scattering.
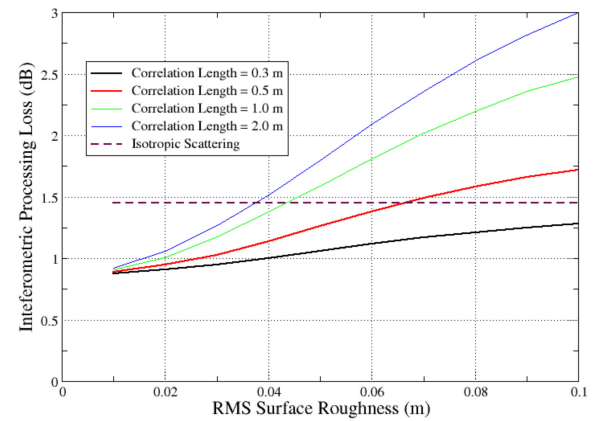

Fig. 14. IPL for the five rough surface cases illustrated in Fig. 13. An antenna gain of 3 dBi is assumed for the direct signal.

characteristics and the corresponding SNR_r will be a spatial average of the SNR_r within the region of integration. We nominally do not observe an rms height of 10 cm within a few meters from any selected point over land surfaces. We can therefore expect that SNR_r for $l_c = 2$ m and $\sigma_h = 0.1$ m is possibly close to the maximum (worst case). The average of SNR_r over correlation length and rms height for the four rough surface cases is 0.7 dB, close to the value for isotropic scattering (–1 dB).

In Fig. 13, we also provide the value of SNR_d, which is 6.6 dB. The direct antenna gain (G_R) of 3 dBi is used for the computation of P_d. We assume that the peak gain of the direct antenna is 6 dBi (see Table I) and the antenna will be slewed so that the MUOS satellite will remain within 3 dB of the direct antenna boresight.

The IPL for the five cases is illustrated in Fig. 14 . The IPL is smaller than 3 dB, and the mean value is close to 2 dB. For comparison, the IPL for isotropic scattering is 0.8 dB. Therefore, we use a value of IPL = 3 dB (see Table I), which would be in general a conversative value, for the evaluation of the overall SNR.

For the SNR computation, the earth-viewing antenna is assumed to have a directivity of 15 dBi, which can be realized by
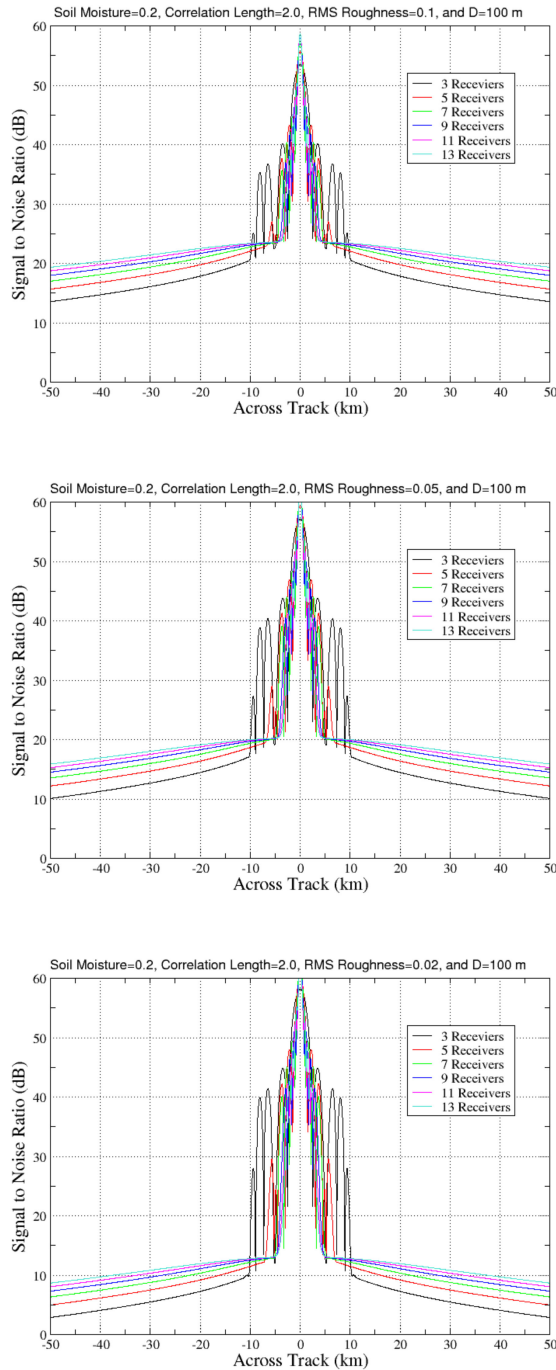
Fig. 15.   SNR versus cross-track distance for three cases: $\sigma_h = 0.1$ m (upper), 0.05 m (middle), and 0.02 m (lower). The correlation length is the same for all three cases, $l_c = 2$ m. A soil moisture of 0.2 and clay fraction of 0.3 are used for simulations. Six curves in each panel are for 3, 5, 7, 9, 11, and 13 receivers, respectively.

a helical antenna with a length of about 4 m and a coil diameter of 30 cm [43]. A deployable helical antenna of a similar size has been developed for the German AISat's Cubesat, operating down to 170 MHz. In the stowed configuration, the AISat antenna helix is compressed to 10 cm in height and 57 cm in diameter[1]. We

[1][Online]. Available: https://spaceflight101.com/spacecraft/aisat/

expect that a similar design can be adapted with frequency tuned for the SoOpSAR.

We have evaluated the SNR for a range of surface roughness conditions (see Fig. 15). The bistatic normalized radar cross section was computed using a Gaussian spatial correlation function for the surface roughness. We find that the coherent term (73) can make a significant contribution near the central portion of swath with an SNR reaching the level of 30 to 60 dB (see Fig. 15). The oscillation in SNR of the coherent term is due to the changing value of F_w (fringe washing) resulting from the effect of integration over Fresnel zones. For a point located far enough from the center of swath, $F_w \approx 0$ and the dominant contribution to the match filter output is the incoherent term (P_{Si}). For $y_c > 30$ km, the spatial resolution is essentially controlled by the range compression as indicated earlier, not the number of receivers. Therefore, the SNR will improve with an increasing number of receivers (M_t). Given the number of receivers considered, the SNR due to incoherent scattering improves rapidly as the number of receivers increases from 3 to 7, but not as much with a further increase.

For rough surfaces with an rms height of 5 cm at the incidence angle of 45°, the SNR can be greater than 10 dB for seven receivers (see Fig. 15). For smoother surfaces (smaller rms height), the incoherent bistatic scattering become smaller, leading to a reduced SNR. The SNR for seven receivers reduces to about 7 dB for an rms height of 2 cm (lower panel of Fig. 15).

Note that the rms height and correlation length considered for numerical illustrations in Fig. 15 are the characteristics of rough surfaces within the spatial resolution of SoOpSAR, about a few hundred meters to 1 km (see Fig. 12). Within the scale of 1 km, an inspection of nominal terrain surfaces suggests that the rms height could be mostly within a few centimeters, which can be supported by the semiempirical analysis based on the CYGNSS data [44]. For a rms height of 5 cm, the Rayleigh parameter, $4k^2\sigma_h^2$, is about 0.6 at the frequency of 360 MHz, and hence, the coherent power, characterized by (76) and (77), can be significant. A Rayleigh parameter of smaller than one leads to a relatively strong coherent reflection and weak diffused scattering; therefore, a high SNR due to coherent scattering can be expected near the center of swath (see Fig. 15). For a rougher surface with an rms height of 10 cm (top panel of Fig. 15), the Rayleigh parameter increases, leading to an increase in the diffused scattering; hence, the SNR can reach 13 dB for as few as three receivers at 50 km off the center of the swath.

E. Ionospheric Impact

The impact of ionosphere on P-band SAR imaging has been investigated in the past two decades, e.g., [45], [46]. The spatial and temporal variations of phase shift due to ionospheric turbulence, which is inversely proportional to radio frequency, can cause performance degradation in resolution, peak power, and sidelobe levels, resulting from defocusing in both range and along-track directions. Liu *et al*. [45] analyzed the SAR image degradation due to an inhomogeneous ionosphere; they conducted simulations of SAR image distortions primarily at 500 MHz, but also at 300, 400, 500, 600, 700, and 1000 MHz

for an average of five TECU and 10% perturbations; they determined that an SAR imaging positional offset of 60 m can be caused by a horizontal gradient of two TECU/10 km. Their analyses are not specific to any particular selection of satellite orbits or local times.

Because of the close proximity of the ESA BIOMASS mission and MUOS-based *P*-band SoOpSAR concept in frequency, dwell time, and local time (dawn/dusk orbits), we will leverage the analyses conducted for the BIOMASS to provide an indication of the ionospheric effects on the SoOpSAR concept.

A detailed impact assessment of ionospheric irregularities on the ESA BIOMASS SAR mission has been conducted by Rogers *et al.* [46], specifically for its dawn/dusk orbits, which turn out to be favorable for the coherent processing required by SAR. The 3-dB beamwidth of the BIOMASS antenna is about 22.6 km, thus allowing a dwell time of about 3 s for synthetic aperture processing, which is in the range of dwell time considered for the SoOpSAR concept (see Table I). The operation frequency of the BIOMASS is 435 MHz, close to the upper MUOS frequency band of 360 MHz. The frequency ratio is about 1.2, suggesting that the SoOpSAR will experience a larger phase shift and, hence, a worsen beam squinting and focusing performance.

Several SAR performance metrics, including the spatial resolution, absolute peak drop (APD), peak sidelobe ratios (PSLRs), integrated sidelobe ratios (ISLRs), and a beam squinting, have been assessed by for BIOMASS [46]. They examined the impact of the ionospheric irregularities by completing a set of simulations using a climatological ionospheric wide band model [47] for the BIOMASS system configuration over a range of ionospheric conditions. Three levels of sunspot numbers, Rz12 = 22, 63, and 106 (quartiles for solar cycles 20–23), and four days of the year (equinoxes, summer, and winter solstices) were considered, therefore leading to results for optimistic, average, and near worst case scenarios. Rogers *et al.* [46] find that for a dawn–dusk (6 AM/PM local time) orbit, impacts of ionospheric scintillation are negligible under nearly all conditions except at high latitudes (north of 45° N) in the North America under high sunspot activity. The influence over high latitudes in the Eurasia is much less over regions to the south of 60° N. The worser performance over North America than Eurasia is due to the offset of the geomagnetic poles toward the North America, hence higher geomagnetic latitudes than Eurasia. For the dawn–dusk orbits, the degradation in the mean 3-dB resolution of up to 10% is predicted for BIOMASS, with mean absolute azimuth shifts of point target response peak of up to 2 m, which increases to 5 m at high sunspot number. Translating these results to the MUOS frequency of 360 MHz with an additional 20% relative phase shift, the beam squinting, which is linearly related to the phase shift, will remain below 6 m for SoOpSAR, which is negligible with respect to the spatial resolution requirement of 100 m–1 km for RZSM and snow remote sensing.

The drop in peak power will have a quadratic dependence on the phase uncertainties and, hence, we can expect a relative degradation of 40% at 360 MHz. Based on [46, Table 3], we can infer that the reduction in peak power at 360 MHz will be less than 0.3 dB for latitude to 45° N in North America and less than 2 dB at 50° N. As indicated earlier, the expected performance
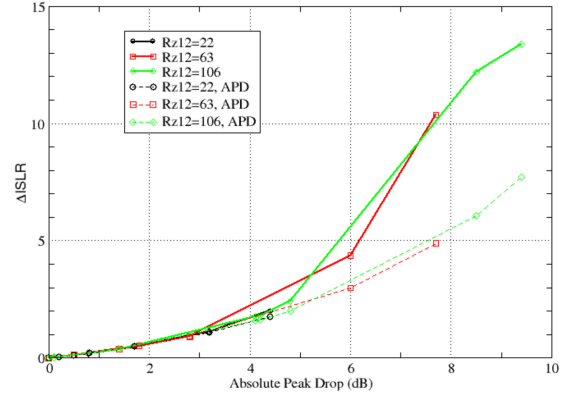

Fig. 16. Relation between APD and ISLR based on the results in [46] for the BIOMASS mission for a range of sunspot numbers (Rz12), corresponding to three quartiles for solar cycles 20–23.

over Eurasia will be better. We can therefore expect that the performance of SoOpSAR at 360 MHz will be degraded by the ionosphere, but can remain acceptable for up to 45° N or higher for a range of ionospheric conditions.

It should be noted that the APD, ISLR, and PSLR are related to each other. The ionospheric irregularities will cause phase fluctuations and, hence, SAR processing to be defocused, leading to a drop in APD. The reduction in peak power will lead to an increase in ISLR because of power conservation. We will use the results in [46] to demonstrate the relationship between APD and ISLR.

We can leverage the results published in [46] for BIOMASS to estimate the expected impact of ionosphere at 360 MHz. The APD is related to the variance of phase changes (σ_ϕ^2) caused by the ionosphere irregularities

$$\text{APD} = e^{-\sigma_\phi^2}. \tag{95}$$

The change of ISLR (ΔISLR) is the difference between the ISLR impacted by the ionosphere and the ideal ISLR of –9.9 dB caused by other factors for BIOMASS. We compute the difference in real values, not the difference of values in decibel. Due to power conservation, when the change is small enough, the delta change in ISLR can be related to the APD by

$$\Delta \text{ISLR}_{\text{APD}} = \frac{1 - \text{APD}}{\text{APD}}. \tag{96}$$

The denominator is the reduced peak power lever and the numerator is the increase in sidelobe power. We use the values of BIOMASS ISLR and APD in [46, Table 3] to compute the ΔISLR and ΔISLR$_{\text{APD}}$ for BIOMASS. They are illustrated versus APD for three levels of sun spots in Fig. 16. It is demonstrated that the relationship between APD and change in ISLR can be characterized by (96) for an APD of up to 3 dB.

We can then apply (95) and (96) for the estimate of APD and ISLR at the frequency of 360 MHz; we compute σ_ϕ^2 from the APD of BIOMASS; then the expected phase variance at 360 MHz is amplified by 40% degradation and computed as $1.4\sigma_\phi^2$. From (95) and (96), we can compute the APD and ΔISLR at 360 MHz.
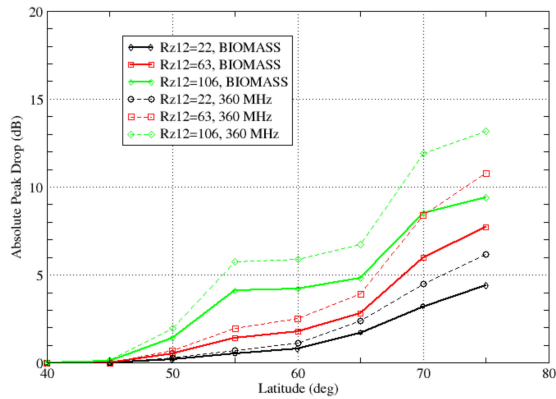
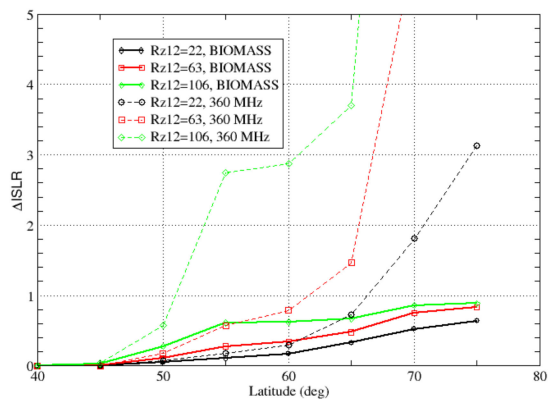Fig. 17.   Estimate of APD at 360 MHz based on the BIOMASS analyses [46].

Fig. 18.   Estimate of delta ISLR at 360 MHz based on the BIOMASS analyses [46].

Figs. 17 and 18 illustrate the APD and IRSL, respectively, at the 435 MHz (BIOMASS) and 360 MHz (SoOpSAR) versus latitude at 110° W (North America). We find that there is a degradation of APD at a lower frequency, but the changes of APD from 435 to 360 MHz are smaller than 1 dB to the south of 50° N. The degradation of ISLR is also negligible for south of 45° N, but the degradation becomes substantial for the top quartile of sun spots (Rz12 = 106) at high latitudes (north of 50° N).

Our results leveraging the analyses of the BIOMASS study suggests a promising performance of the SoOpSAR for a range of latitudes and ionospheric conditions for dawn/dusk orbits. We will however suggest that this issue deserves a further analysis for the SoOpSAR using updated ionosphere TEC models in the future.

We can anticipate that the impact of ionospheric TEC can possibly be reduced by using the ionospheric TEC model for SAR data correction or processing. The GNSS-based TEC products and ionospheric models are expected to improve in spatial and temporal sampling in the future due to the expansion in GNSS satellite networks, including 24 satellites in the US global positioning systems (GPSs), 35 satellites in the Chinese BeiDou Navigation Satellite System, 24 satellites in the European Union's Galileo system, 24+ satellites in the Globalnaya

Navigazionnaya Sputnikovaya Sistema operated by the Russian Federation, and 7 satelllites in the Indian Regional Navigation Satellite System. The phase change due to TEC can be computed from the GNSS TEC data and models and introduced into the match filtering of SoOpSAR focusing. The dual-frequency data from MUOS (260 and 360 MHz channels or two 10-MHz subbands in the 360-MHz channel) can also be explored to improve estimation of the STEC and, hence, focusing. Further research should be explored to reduce the impact of ionosphere and extend useful coverage of SoOpSAR toward high latitudes.

V. MUOS TRANSMIT SIGNALS

A. Autocorrelation

We have analyzed the autocorrelation of MUOS transmit signals to determine whether there could be embedded signals that may introduce ambiguities by range compression. MUOS operates two channels, one from 240 to 270 MHz and the other one from 360 to 380 MHz. There are four subchannels with a bandwidth of 5 MHz for each at the 360-MHz band. The autocorrelation of MUOS signals at 360 MHz for one subchannel is illustrated in Fig. 19 and three subchannels in Fig. 20. There are repeatable peaks at 0.01-s intervals, which could be related to the spectrally adaptive wideband code division multiple access waveform adapted by MUOS for the 360-MHz band [25]. Using the data from three subchannels reduces the secondary peak at 0.01 s to about 5 dB below the primary peak. The width of the primary peak for three subchannels reaches about 0.1 μs (right panel of Fig. 20).

The secondary peak at 0.01 s will introduce slant range ambiguities after range compression. This secondary peak corresponds to a range delay of 3000 km and will be far from the center of processing area. For $\theta = 45°$, the location on the earth corresponding to the range delay of 3000 km will be either in the shadow of the earth (e.g., point B in Fig. 21), not visible by the receiving LEO satellite, or will have its reflection entering the back lobe (i.e., θ_a greater than 90° from the boresight) of the receiving antenna (e.g., point A in Fig. 21). The reflected signal with the 0.01-s delay will either not be able to reach the receive satellite or will be very small due to low surface scattering at high incidence and scattering angles (θ_s) and low antenna gain for far-side and back lobes. Similar conclusions can be drawn for other incidence angles (left panel of Fig. 21). For θ very close to 0°, all points related to the 0.01 s excess delay will have their scattering coming from very low grazing angles (or local scattering angle near 90°). We can therefore conclude that the coding of MUOS transmit signals allows the SAR processing with negligible range ambiguities due to some periodicity in the transmit signals.

B. Transmit Power Level

The transmit power level of MUOS was found to be relatively stable based on the data collected from a field campaign at Fraser, CO, USA [34], [36]. The campaign was carried out to demonstrate the use of P-band reflectometry for snow and RZSM remote sensing. The instrumentation has included an antenna
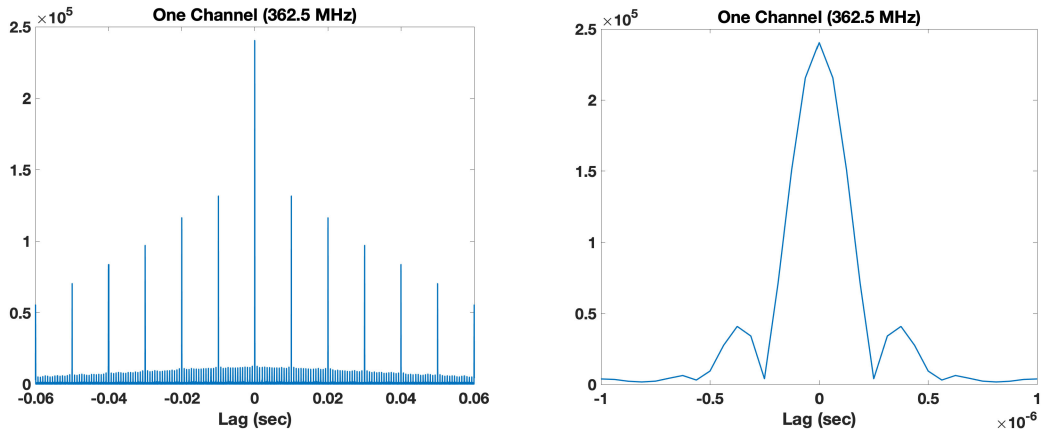
Fig. 19. Autocorrelation of MUOS transmit signal at 362.5 MHz with 5-MHz bandwidth for one channel. There is some repeatability every 0.01 s (left panel). Zoom-in of the autocorrelation near zero lag (right panel) has a well-defined peak with the level of first sidelobe about 7 dB below peak.
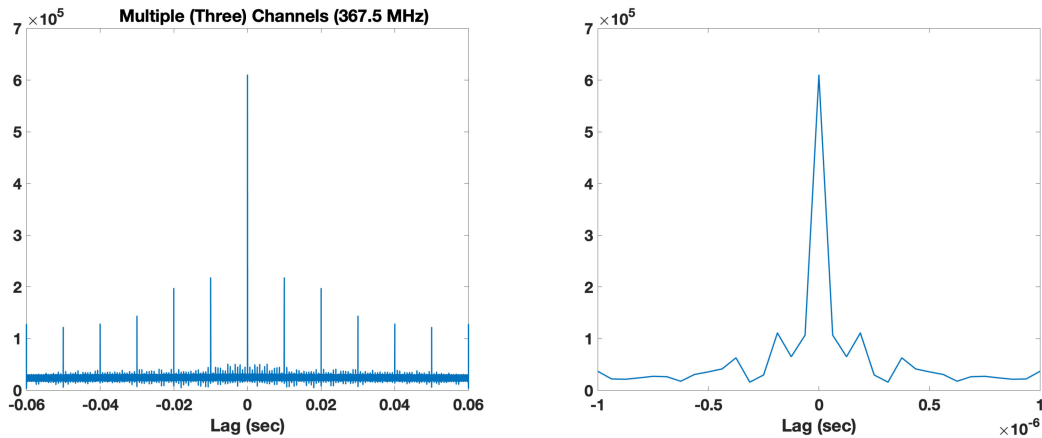

Fig. 20. Autocorrelation of MUOS transmit signal with a center frequency of 367.5 MHz and a bandwidth of 15 MHz for three channels. There is some repeatability every 0.01 s (left panel). Zoom-in of the autocorrelation near the zero lag has a well-defined peak with the level of first sidelobe about 8 dB below peak.
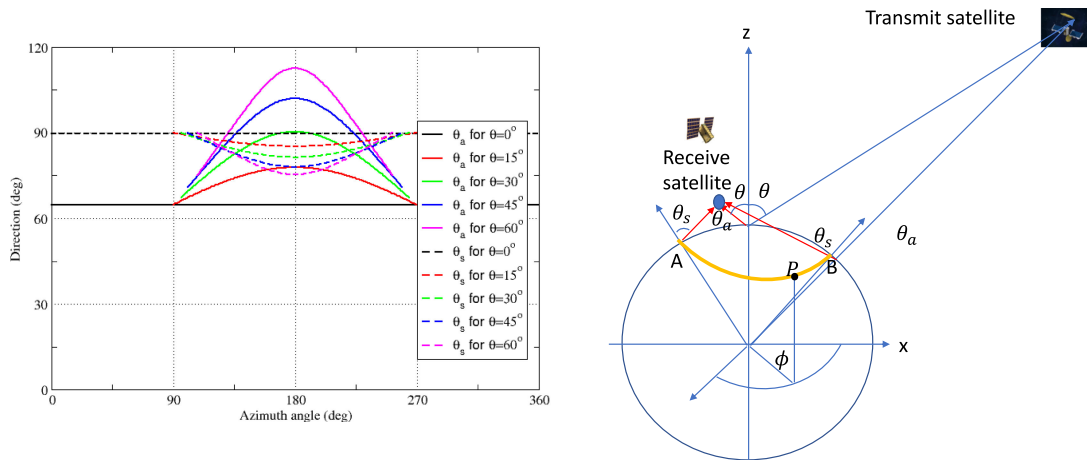

Fig. 21. Left panel: Scattering angle (θ_s) and receiving direction from the antenna boresight (θ_a) for five different incidence angles (θ) versus azimuth angle ϕ. Right panel: Gold contour represents the iso-range corresponding to the 0.01-s delay. Point B is in the shadow of earth, whereas point A (azimuth angle = 180°) has θ_a reaching 105°.
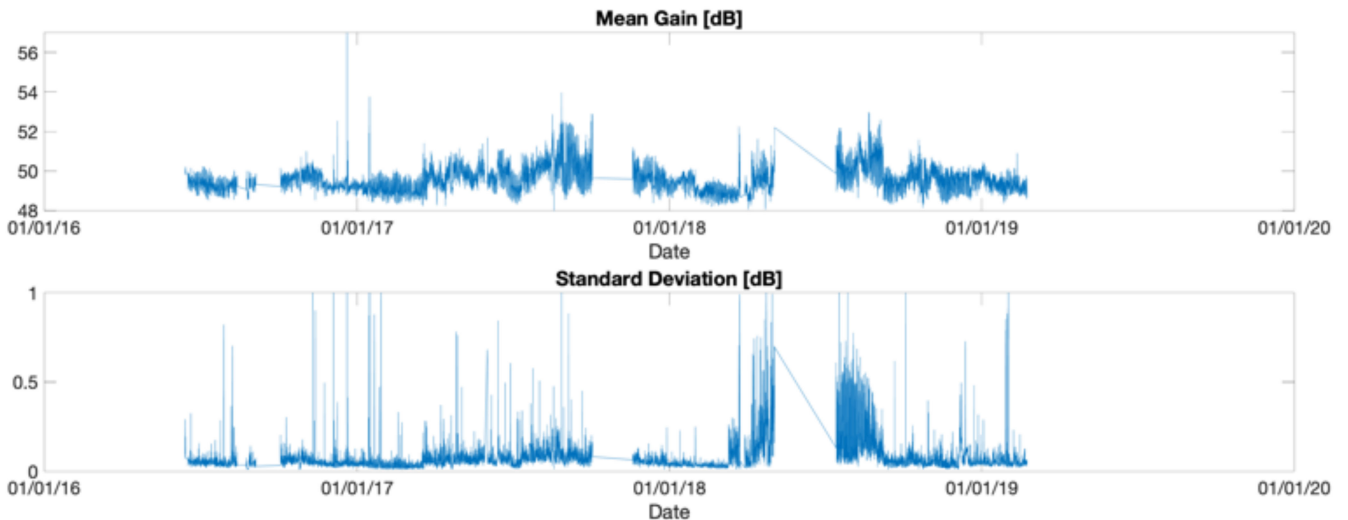
Fig. 22.   Transmit power of MUOS recorded during a field experimental conducted at Fraser, CO, USA, from 2016 to early 2019. (Upper panel) the mean power level in decibel over a 10-min window recorded by the receiver is plotted versus time. Our receiver does not have a built-in radiometric calibration reference to allow us to verify the MUOS EIRP of 43 dBW. The illustrated value includes the antenna and receiver gains of our instrument. (Lower panel) standard deviation of the 0.5-s integrated power levels within 10 min.

pointing toward the MUOS satellite to acquire the direct signal. Fig. 22 illustrates the characteristics of transmit power level for about three years whenever the ground-based receiver was ON (the receiver was down sometimes for repair and maintenance.). We collected 20 s of data over 10 min every 3 h at Fraser. The data from every 0.5-s interval have been used to compute a power level; hence, there are 40 0.5-s samples within the 10-min window for the computation of mean and standard deviation of transmit power. The mean power level was mostly within plus and minus 1 dB over three years. The standard deviation was mostly less than 0.1 dB, but sometimes could reach 1 dB. The overall mean of the standard deviation is 0.09 dB. The data suggest that the MUOS transmit source is mostly stable for SoOpSAR although accounting for the temporal changes is clearly necessary for radiometric calibration.

VI. KEY TECHNOLOGY CONSIDERATIONS

There are at least two key technology issues for the proposed spaceborne SoOpSAR concept. One is the formation flight technology for a fleet of small satellites, and the other one is the relative timing to enable the coherent processing of signals from multiple satellites. We will discuss the issues here, and recommend future technology studies to enable the implementation of SoOpSAR.

A. Formation Flight of Small Satellites

The spacing between receivers will affect the array factor, including the locations of major ambiguities and sidelobe levels. It is unnecessary to control the spacing to be exactly 100 m apart. We can compute the locations of ambiguities and sidelobe levels as long as we know the position of receivers. The state-of-the-art satellite position accuracy based on GPS technologies is < 5 cm, which will allow us to compute the array factor accurately at the P-band frequency. If the spacing is nonuniform, the sidelobe and

ambiguity level will change. Once we determine the location of ambiguities, the portion of swath with a significant ambiguity ratio can be identified and flagged.

The state-of-the-art SAR satellite orbit management is being performed by the needs for repeat pass SAR interferometry. The European Sentinel-1 SAR mission has shown an orbital control within a tube of about 50 m (rms) [48], which is comparable to the baseline spacing of 50 or 100 m used for the SoOpSAR concept, and hence remains inadequate.

A relevant technology demonstration on precision orbital control of nanosatellites has been shown by the CanX-4 and CanX-5 mission that a control accuracy of 1 m is feasible [49]. The mission brought two satellites from a maximum range of 2300 km to a closest controlled range of 50 m by using onboard propulsion system, differential GPS technologies for satellite precision orbit determination (POD), and intersatellite S-band communication links for autonomous orbit maneuvers. The results are promising for SoOpSAR. However, the next step will require a demonstration that the orbit management can be performed consistently over a long duration (years) with an acceptable amount of onboard fuel storage required for thruster control.

A deviation of the receiver positions from a uniform spacing will cause a change to the sidelobes of the array factor characterized by (52). Suppose that the mth receiver moves off its nominal position y'_m by a distance of δ_m, the resulting change in phase will be

$$\varphi_m = \frac{2\pi}{\lambda} \frac{\delta_m}{R_{0r}} \left(y'_p - y'_{pc} \right). \qquad (97)$$

For the geometry based on the parameters indicated in Table I, $R_{0r} \approx 900$ km, the phase change will be less than $5°$ for $|\delta_m| < 1$ m and $|y'_p - y'_{pc}| < 10$ km, and hence will have a negligible impact on the array factor A_p. We can conclude that if the position of receivers can be controlled to within 1 m, as demonstrated
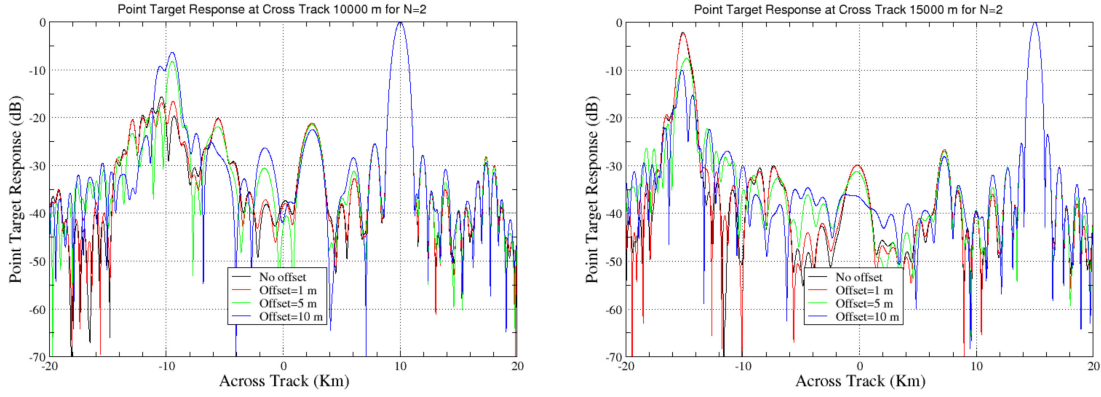
Fig. 23. Point target response versus the cross-track distance for an offset of $\delta = 1$ m, 5 m, and 10 m for five receivers ($M = 2$). (Left panel) the target is located at $y_c = 10$ km; (Right panel) the target is located at $y_c = 15$ km.

by CanX-4/-5, then the point target response of SoOpSAR will essentially not be affected.

To illustrate the impact of displacement on P_{TR}, we computed the PTR for a few cases with displacement of satellite position characterized by

$$\delta_m = \delta(-1)^m \qquad (98)$$

if m is not zero. Without loss of generality, we let $\delta_0 = 0$ because the array factor is determined by the relative position of receivers. Fig. 23 illustrates the point target response versus the cross-track distance for an offset of $\delta = 1$, 5, and 10 m for five receivers ($M = 2$). The numerical examples confirm that P_{TR} is essentially unaffected for $\delta = 1$ m. For a larger offset of 5 and 10 m, P_{TR} near the focal point remains unaffected; however, the far sidelobes may increase or decrease. It is interesting to notice that the sidelobe level near the mirror ambiguity may decrease to -10 dB from 3 dB for $y_c = 15$ km and $\delta = 10$ m (right panel in Fig. 23), whereas the sidelobe level near the mirror ambiguity may actually increase from -17 to -7 dB for $y_c = 10$ km and $\delta = 10$ m (left panel in Fig. 23). Thus, the sidelobe performance can still be acceptable for a displacement as large as 10 m. However, a precision orbit management of 1 m in accuracy is clearly desirable.

B. Relative Timing

We envision that the timing of each SoOpSAR satellite can be tied to the GPS clock by including GPS receivers onboard for POD of the SoOpSAR. The state-of-the-art GPS POD for LEO satellite is about 4 cm. This corresponds to a timing accuracy of about 0.1 ns. The resulting phase uncertainty at the center frequency (360 MHz) of the SoOpSAR will be about 15°. A random phase will lead to a degradation of the array factor gain characterized by (52) by only about 0.2 dB based on (90). However, if the SoOpSAR concept is to be considered for higher frequency sources, such as *Ku-* and *Ka*-band used for satellite television services, then the clocking error has to be much greatly improved.

VII. SUMMARY

We have completed an analysis to indicate the potential of using *P*-band MUOS SoOp signals for synthetic aperture imaging of land surfaces. It is shown that SoOp radar can be combined with the multistatic sparse array technique to achieve high spatial resolution and adequate ambiguity performance for a large portion of swath. The analysis of SNR was completed based on the KA for surface scattering, indicating the ability of SoOpSAR concept to achieve an SNR of better than a few decibels with a moderate antenna directivity of 15 dBi for a wide range of surface roughness conditions and a potential swath width of 100 km or larger. The effects of ionosphere are analyzed by leveraging the results obtained for the BIOMASS mission and suggest that SoOpSAR can operate over a range of latitudes and ionospheric conditions for dawn/dusk orbits. Impact of ionosphere for other local times could be more severe, and will definitely require a more detailed analysis. Key technology issues, including formation flights of small satellites and receiver timing, were discussed and recommended for technology development in order to realize the *P*-band SoOpSAR concept in space.

APPENDIX A
POLARIMETRIC SCATTERING COEFFICIENTS FOR KA

The scattering coefficients for linear polarizations are given in [37, pp. 82 and 83]. We can obtain the coefficients for circulation polarizations from them by

$$\begin{bmatrix} F_{RR} & F_{RL} \\ F_{LR} & F_{LL} \end{bmatrix} = \frac{1}{2} \begin{bmatrix} 1 & -i \\ 1 & i \end{bmatrix} \begin{bmatrix} F_{vv} & F_{vh} \\ F_{hv} & F_{hh} \end{bmatrix} \begin{bmatrix} 1 & 1 \\ i & -i \end{bmatrix} \qquad (A1)$$

where

$$F_{hh} = \frac{1}{2} \left[(1 - R_H) \cos\theta_i - (1 + R_H) \cos\theta_s \right] \cos(\phi_s - \phi_i)$$

$$F_{vh} = \frac{1}{2} \left[(1 - R_H) \cos\theta_s \cos\theta_i - (1 + R_H) \right] \sin(\phi_s - \phi_i)$$

$$F_{hv} = \frac{1}{2} \left[(1 + R_V) - (1 - R_V) \cos\theta_s \cos\theta_i \right] \sin(\phi_s - \phi_i)$$

$$F_{vv} = \frac{1}{2} \left[-(1 + R_V) \cos\theta_s + (1 - R_V) \cos\theta_i \right] \cos(\phi_s - \phi_i).$$

R_H and R_V are Fresnel reflection coefficients for horizontal and vertical polarizations, respectively, for incidence angle θ_i. F_{vv}, F_{hh}, F_{hv}, and F_{vh} in the aforementioned equations are one-half as they are defined in [37].

APPENDIX B
INTERFEROMETRIC PROCESSING LOSS

The direct signal with noise can be modeled for the mth satellite receiver by

$$E_{dm}(t) = g(\bar{r}_{dm}) \lambda a' \left(t - \frac{r_{dm}}{c} \right) \frac{e^{-ikr_{dm}}}{r_{dm}} e^{i2\pi f_c t} \quad \text{(B1)}$$

with the contaminated transmit waveform described as

$$a' \left(t - \frac{r_{dm}}{c} \right) = a \left(t - \frac{r_{dm}}{c} \right) + b_m(t). \quad \text{(B2)}$$

Here, $b_m(t)$ is due to the thermal noise in the direct receiver. Its expected power is the inverse of SNR of the direct signal

$$\left\langle |b_m|^2 \right\rangle = \frac{1}{\text{SNR}_{Dm}} = \frac{k_B T_{Dm} B_m}{P_{Dm}}. \quad \text{(B3)}$$

The power of the noise-free direct signal is

$$P_{Dm} = \frac{P_T G_T G_R}{4\pi r_{Dm}^2} \frac{\lambda^2}{4\pi}. \quad \text{(B4)}$$

Using the noisy waveform for the match filtering and following the same derivation shown in [41], we can show that the expected power of match filter output contains two additional noise-related terms

$$\langle |S'|^2 \rangle = P_S + P_N + P_{DN} + P_{Dr}. \quad \text{(B5)}$$

They are the third and fourth terms in the aforementioned equation and expressed by

$$P_{DN} = \frac{k_B}{M_t^2 N_r T_w} \sum_m \frac{|A_m|^2 T_{rm}}{\text{SNR}_{Dm}} \quad \text{(B6)}$$

$$P_{Dr} = \frac{k_B}{M_t^2 N_r T_w} \sum_m \frac{|A_m|^2 T_{rm}}{\text{SNR}_{Dm}} \text{SNR}_{Rm} \quad \text{(B7)}$$

where the SNR of reflected signal prior to the match filtering is

$$\text{SNR}_{Rm} = \frac{P_{Rm}}{k_B T_{rm} B_m}. \quad \text{(B8)}$$

The bandwidth of the mth receiver is denoted by B_m and the power of reflected signal is P_{rm}, which can be computed by the equation of bistatic radar equation (92).

Given the aforementioned expressions, the SNR of the match filter output using the noisy waveform is

$$\text{SNR} = \frac{\text{SNR}_c}{\text{IPL}} \quad \text{(B9)}$$

where the IPL is

$$\text{IPL} = 1 + \frac{P_{DN}}{P_N} + \frac{P_{Dr}}{P_N}. \quad \text{(B10)}$$

If we assume the same receiver bandwidth, receiver noise temperature, and antenna gain for receivers on all satellites, the expression of IPL will reduce that shown in [41].

REFERENCES

[1] D. Entekhabi and M. Moghaddam, "Mapping recharge from space: Roadmap to meeting the grand challenge," *Hydrogeology J.*, vol. 15, pp. 105–116, 2007.

[2] Le Toan *et al.*, "The BIOMASS mission: Mapping global forest biomass to better understand the terrestrial carbon cycle," *Remote Sens. Environ.*, vol. 115, no. 11, pp. 2850–2860, Nov. 2011.

[3] Accessed: Dec. 22, 2020. [Online]. Available: https://directory.eoportal.org/web/eoportal/satellite-missions/b/biomass

[4] H. Rott *et al.*, "Cold regions hydrology high-resolution observatory for snow and cold land processes," *Proc. IEEE*, vol. 98, no. 5, pp. 752–765, May 2010.

[5] T. Painter *et al.*, "The airborne snow observatory: Fusion of scanning lidar, imaging spectrometer, and physically-based modeling for mapping snow water equivalent and snow albedo," *Remote Sens. Environ.*, vol. 184, pp. 139–152, Oct. 2016.

[6] T. Guneriussen, K. A. Høgda, H. Johnsen, and I. Lauknes, "InSAR for estimation of changes in snow water equivalent of dry snow," *IEEE Trans. Geosci. Remote Sens.*, vol. 39, no. 10, pp. 2101–2108, Oct. 2001

[7] E. Deeb, R. R. Forster, and D. L. Kane, "Monitoring snowpack evolution using interferometric synthetic aperture radar on the North Slope of Alaska, USA," *Int. J. Remote Sens.*, vol. 32, no. 14, pp. 3985–4003, 2011.

[8] S. Leinss, A. Wiesmann, J. Lemmetyinen, and I. Hajnsek, "Snow water equivalent of dry snow measured by differential interferometry," *IEEE J. Sel. Topics Appl. Earth Observ. Remote Sens.*, vol. 8, no. 8, pp. 3773–3790, Aug. 2015.

[9] S. Katzberg, O. Torres, M. S. Grant, and D. Masters, "Utilizing calibrated GPS reflected signals to estimate soil moisture reflectivitiy and dielectric constant: Results from SMEX02," *Remote Sens. Environ.*, vol. 100, pp. 17–28, 2005.

[10] N. Rodriguez-Alvarez *et al.*, "Soil moisture retrieval using GNSS-R techniques: Experimental results over a bare soil field," *IEEE Trans. Geosci. Remote Sens.*, vol. 47, no. 11, pp. 3616–3624, Nov. 2009.

[11] N. Rodriguez Alvarez *et al.*, "Review of crop growth and soil moisture monitoring from a ground-based instrument implementing the interference pattern GNSS-R technique," *Radio Sci.*, vol. 46, no. 6, pp. 1–11, Dec. 2011.

[12] N. Rodriguez-Alvarez *et al.*, "Land geophysical parameters retrieval using the interference pattern GNSS-R technique," *IEEE Trans. Geosci. Remote Sens.*, vol. 49, no. 1, pp. 71–84, Jan. 2011.

[13] A. Egido *et al.*, "Airborne GNSS-R polarimetric measurement for soil moisture and above ground biomass estimation," *IEEE J. Sel. Topics Appl. Earth Observ. Remote Sens.*, vol. 7, no. 5, pp. 1522–1532, May 2014.

[14] A. Camps *et al.*, "Sensitivity of GNSS-R spaceborne observations to soil moisture and vegetation," *IEEE J. Sel. Topics Appl. Earth Observ. Remote Sens.*, vol. 9, no. 10, pp. 4730–4742, Oct. 2016.

[15] C. Chew, R. Shah, C. Zuffada, G. Hajj, D. Masters, and A. Mannucci, "Demonstrating soil moisture remote sensing with observationsfrom the UK TechDemoSat-1 satellite mission," *Geophys. Res. Lett.*, vol. 43, no. 7, pp. 3317–3324, 2016, doi: 10.1002/2016GL068189.

[16] A. Camps, M. Vall-llossera, H. Park, G. Portal, and L. Rossato, "Sensitivity of TDS-1 GNSS-R reflectivity to soil moisture: Global and regional differences and impact of different spatial scales," *Remote Sens.*, vol. 10, 2018, Art. no. 1856.

[17] N. Rodriguez-Alvarez, S. Misra, E. Podest, M. Morris, and X. Bosch-Lluis, "The use of SMAP-reflectometry in science applications: Calibration and capabilities," *Remote Sens.*, vol. 11, 2019, Art. no. 2442.

[18] N. Rodriguez-Alvarez, S. Misra, and M. Morris, "The polarimetric sensitivity of SMAP-reflectometry signals to crop growth in the U.S. Corn Belt," *Remote Sens.*, vol. 12, 2020, Art. no. 1007.

[19] C. S. Ruf *et al.*, "The CYGNSS nanosatellite constellation hurricane mission," in *Proc. IEEE Int. Geosci. Remote Sens. Symp.*, Jul. 2012, pp. 214–216.

[20] C. C. Chew and E. E. Small, "Soil moisture sensing using spaceborne GNSS reflections: Comparison of CYGNSS reflectivity to SMAP soil moisture," *Geophys. Res. Lett.*, vol. 45, pp. 4049–4057, 2018. [Online]. Available: https://doi.org/10.1029/2018GL077905

[21] M. M. Al-Khaldi, J. T. Johnson, A. J. O'Brien, A. Balenzano, and F. Mattia, "Time-series retrieval of soil moisture using CYGNSS," *IEEE Trans. Geosci. Remote Sens.*, vol. 57, no. 7, pp. 4322–4331, Jul. 2019.

[22] G. A. Hajj and C. Zuffada, "Theoretical description of a bistatic system for ocean altimetry using the GPS signal," *Radio Sci.*, vol. 38, no. 5, pp. 10-1–10-19, 2003.

[23] A. Camps, "Spatial resolution in GNSS-R under coherent scattering," *IEEE Geosci. Remote Sens. Lett.*, vol. 17, no. 1, pp. 32–36, Jan. 2020.

[24] V. U. Zavorotny and A. G. Voronovich, "Scattering of GPS signals from the ocean with wind remote sensing application," *IEEE Trans. Geosci. Remote Sens.*, vol. 38, no. 2, pp. 951–964, Mar. 2000.

[25] J. D. Oetting and T. Jen, "The mobile user objective system," *Johns Hopkins APL Tech. Dig.*, vol. 30, no. 2, pp. 103–112, 2011. [Online]. Available: http://techdigest.jhuapl.edu/TD/td3002/Oetting.pdf

[26] X. Xu and S. Yueh, "Multi-frequency bistatic reflectometry over terrestrial snow cover using signals of opportunity," in *Proc. Int. Geosci. Remote Sens. Symp.*, 2015, pp. 1–3.

[27] S. Yueh, R. Shah, X. Xu, K. Elder, and C. Chae, "P-band signals of opportunity for remote sensing of snow and root zone soil moisture," in *Proc. Prog. Electromagn. Res. Symp.*, p. 1, 2017.

[28] J. Garrison *et al.*, "Recent results on soil moisture remote sensing using P-band signals of opportunity," in *Proc. Int. Conf. Electromagn. Adv. Appl.*, 2017, pp. 1604–1607.

[29] J. Garrison *et al.*, "Remote sensing of soil moisture using P-band signals of opportunity (SoOp): Initial results," in *Proc. IEEE Int. Geosci. Remote Sens. Symp.*, 2017, pp. 4158–4161.

[30] X. Xu, R. Shah, S. Yueh, and K. Elder, "Reflectivity modeling of signals of opportunity for remote sensing of snow and soil moisture," in *Proc. IEEE Int. Geosci. Remote Sens. Symp.*, 2017, pp. 1438–1440.

[31] S. Yueh *et al.*, "HydroCube mission concept: P-band signals of opportunity for remote sensing of snow and root zone soil moisture," in *Proc. SPIE*, Sep. 2017, Art. no. 104230L.

[32] J. L. Garrison *et al.*, "Remote sensing of root-zone soil moisture using I- and P-band signals of opportunity: Instrument validation studies," in *Proc. IEEE Int. Geosci. Remote Sens. Symp.*, 2018, pp. 8305–8308.

[33] S. Yueh, X. Xu, R. Shah, S. Margulis, and K. Elder, "P-band signals of opportunity for remote sensing of root zone soil moisture," in *Proc. IEEE Int. Geosci. Remote Sens. Symp.*, 2018, pp. 1403–1406.

[34] R. Shah *et al.*, "Remote sensing of snow water equivalent using P-band coherent detection," *IEEE Geosci. Remote Lett.*, vol. 14, no. 3, pp. 309–313, Mar. 2017.

[35] S. Yueh *et al.*, "Remote sensing of snow water equivalent using coherent reflection from satellite signals of opportunity: Theoretical modeling," *IEEE J. Sel. Topics Appl. Earth Observ. Remote Sens.*, vol. 10, no. 12, pp. 5529–5540, Dec. 2017.

[36] S. Yueh, R. Shah, X. Xu, K. Elder, and B. Starr, Experimental demonstration of soil moisture remote sensing using P-band satellite signals of opportunity, *IEEE Geosci. Remote Sens. Lett.*, vol. 17, no. 2, pp. 207–211, Feb. 2020.

[37] L. Tsang, J. A. Kong, and R. T. Shin, *Theory of Microwave Remote Sensing*. New York, NY, USA: Wiley, 1985.

[38] R. D. De Roo and F. T. Ulaby, "Bistatic specular scattering from rough dielectric surfaces," *IEEE Trans. Antennas Propag.*, vol. 42, no. 2, pp. 220–231, Feb. 1994.

[39] G. Krieger and A. Moreira, "Spaceborne bi- and multistatic SAR: potential and challenges," *IEE Proc.-Radar Sonar Navig.*, vol. 153, no. 3, pp. 184–198, Jun. 2006.

[40] A. Alonso-Arroyo *et al.*, "SNR and standard deviation of cGNSS-R and iGNSS-R scatterometric measurements," *Sensors*, vol. 17, 2017, Art. no. 183.

[41] M. Martin-Neira, "A passive reflectometry and interferometry system (PARIS): Application to ocean altimetry," *ESA J.*, vol. 17, pp. 331–355, 1993.

[42] V. L. Mironov, L. G. Kosolapova, and S. V. Fomin, "Physically and mineralogically based spectroscopic dielectric model for moist soils," *IEEE Trans. Geosci. Remote Sens.*, vol. 47, no. 7, pp. 2059–2070, Jul. 2009.

[43] C.-C. Chen, *Small Antennas: Miniaturization Techniques & Applications*, J. L. Vokalis, C. C. Chen, and K. Fujimoto, Eds. New York, NY, USA: McGraw-Hill, Jul. 2010, ch. 5.

[44] S. Yueh, R. Shah, M. J. Chaubell, A. Hayashi, X. Xu, and A. Colliander, "A semi-empirical modeling of soil moisture, vegetation, and surface roughness impact on CYGNSS reflectometry data," *IEEE Trans. Geosci. Remote Sens.*, to be published, doi: 10.1109/TGRS.2020.3035989.

[45] J. Liu, Y. Kuga, A. Ishimaru, X. Pi, and A. Freeman, "Ionospheric effects on SAR imaging: A numerical study," *IEEE Trans. Geosci. Remote Sens.*, vol. 41, no. 5, pp. 939–946, May 2003.

[46] N. C. Rogers, S. Quegan, J. S. Kim, and K. P. Papathanassiou, "Impacts of ionospheric scintillation on the BIOMASS P-band satellite SAR," *IEEE Trans. Geosci. Remote Sens.*, vol. 52, no. 3, pp. 1856–1868, Mar. 2014.

[47] Y. Béniguel, "GISM global ionospheric scintillation model," Technical Manual, Sep. 2011. [Online]. Available: http://www.ieea.fr/help/gism-technical.pdf

[48] Accessed: Dec. 22, 2020. [Online]. Available: https://directory.eoportal.org/web/eoportal/satellite-missions/c-missions/copernicus-sentinel-1

[49] G. Bonin, N. Roth, S. Armitage, J. Newman, B. Risi, and R. Zee, "CanX-4 and CanX-5 precision formation flight: Mission accomplished!" in *Proc. 29th Annu. AIAA/USU Conf. Small Satell.*, pp. 1–15, 2015.

Simon H. Yueh (Fellow, IEEE) received the Ph.D. degree in electrical engineering from the Massachusetts Institute of Technology, Cambridge, MA, USA, in January 1991.

He was a Postdoctoral Research Associate with the Massachusetts Institute of Technology from February to August 1991. In September 1991, he joined the Radar Science and Engineering Section, Jet Propulsion Laboratory, Pasadena, CA, USA, and has assumed various engineering and science management responsibilities. He served as the Project Scientist of the National Aeronautics and Space Administration (NASA) Aquarius mission from January 2012 to September 2013, the Deputy Project Scientist of NASA Soil Moisture Active Passive Mission from January 2013 to September 2013, and has been the SMAP Project Scientist since October 2013. He has been the Principal/Co-Investigator of numerous NASA and DOD research projects on remote sensing of ocean salinity, ocean wind, terrestrial snow, and soil moisture. He has authored four book chapters and authored or coauthored more than 200 publications and presentations.

Dr. Yueh was the recipient of the 2014 IEEE GRSS Transaction Prize Paper Award, 2010 IEEE GRSS Transaction Prize Paper Award, 2002 IEEE GRSS Transaction Prize Paper Award, the 2000 Best Paper Award in the IEEE International Geoscience and Remote Symposium 2000, and the 1995 IEEE GRSS Transaction Prize Paper Award for a paper on polarimetric radiometry. He was also the recipient of the JPL Lew Allen Award in 1998, JPL Ed Stone Award in 2003, NASA Exceptional Technology Achievement Award in 2014, and NASA Outstanding Public Leadership Medal in 2017. He was an Associate Editor for the *Radio Science* from 2003 to 2007. He is a member of the American Geophysical Union, an Editor-in-Chief for the IEEE TRANSACTIONS ON GEOSCIENCE AND REMOTE SENSING, and a member of URSI Commission F.

Rashmi Shah (Senior Member, IEEE) received the B.S. degree in electrical engineering from the Rochester Institute of Technology, Rochester, NY, USA, in 2007, and the M.S. and Ph.D. degrees in aeronautical and astronautical engineering from Purdue University, West Lafayette, IN, USA, in 2010 and 2014, respectively.

Since 2014, she has been with Jet Propulsion Laboratory, California Institute of Technology, Pasadena, CA, USA, as a Research Technologist with the Tracking Systems and Applications Section. She is also part of the core team member for JPL Foundry's A-team where she works with teams on early concept development. Her background and interests include microwave remote sensing, electromagnetic scattering, remote sensing using signals of opportunity reflectometry, and microwave remote sensing instrument development.

Dr. Shah was the recipient of NASA Early Career Public Achievement Medal and Institute of Electrical and Electronics Engineers (IEEE) Geoscience and Remote Sensing Society's (GRSS) Early Career Award. She serves as a Co-Chair of GNSS and Signals of Opportunity Working Group for the IEEE GRSS Society's Instrumentation and Future Technologies Technical Committee. She also serves as a Chapter Chair for the IEEE Metropolitan Los Angeles GRSS Chapter.

Xiaolan Xu received the B.Eng. degree from Zhejiang University, Hangzhou, China, in 2006, and the M.S. and Ph.D. degrees in electrical engineering from the University of Washington, Seattle, WA, USA, in 2008 and 2011, respectively.

In 2012, she joined the Jet Propulsion Laboratory, California Institute of Technology, Pasadena, CA, USA, as a Postdoctoral Research Associate and has been a Scientist since 2014. Her expertise is in the field of applied electromagnetics, electromagnetic wave propagation and scattering properties from snow covered terrain, vegetated land surface and bare soil, forward modeling, and retrieval algorithm development with applications to earth remote sensing in space.

Dr. Xu was the recipient of the URSI Santimay Basu Prize in 2020 for her work on wave propagation and scattering in dense random media with applications to microwave remote sensing of snow.

Bryan Stiles received the Ph.D. degree in electrical engineering from The University of Texas at Austin, Austin, TX, USA, in 1997.

Since 1997, he has been with NASA's Jet Propulsion Laboratory (JPL), Pasadena, CA, USA. At JPL, he has developed simulations, ground processing, and data analysis algorithms for spaceborne radar. He led the development of the synthetic aperture radar (SAR) processor and the point target simulator for the Cassini Radar instrument. He has employed Cassini SAR data to estimate the location of the spin axis of Titan and to determine the topography of its surface. In addition to his work on Cassini, he has worked on the end-to-end simulation of ocean wind scatterometers and developed algorithms for estimating geophysical values from scatterometer data. He developed a means for improving the wind retrieval accuracy of pencil beam scanning scatterometers that is employed today by NASA and NOAA in processing QuikSCAT data. He also developed a statistical model of the impact of rain on ocean wind scatterometer data that is used to flag for rain contamination.

Xavier Bosch-Lluis received the B.S. and M.S. degrees in telecommunications engineering from the Universitat Politecnica de Catalunya, Barcelona, Spain, in 2005 and 2009, respectively, and the Ph.D. degree in remote sensing from the Department of Signal Theory and Communications, Universitat Politecnica de Catalunya, in 2011.

He was a Postdoc with the Department of Electrical and Computer Engineering, Microwave Systems Laboratory (MSL), Colorado State University, Fort Collins, CO, USA. At the MSL, he was with the High Frequency Airborne Microwave and Millimeter-Wave Radiometer instrument to demonstrate increased spatial resolution of wet tropospheric path delay retrieval for high-resolution ocean surface altimeter missions. He was also with the Tropospheric Water and Cloud Ice Instrument, designed for operation in a 6U CubeSat, with the scientific goal of providing global measurements of upper tropospheric water vapor as well as cloud ice particle size distribution and total cloud ice water content variability. He is currently a Technologist with the Microwave Systems Technology Group, Jet Propulsion Laboratory, California Institute of Technology, Pasadena, CA, USA. His research interests include autonomous instruments by artificial intelligence, microwave and millimeter-wave radiometer design and calibration, as well as innovative digital radiometric concepts, such as digital beamforming or polarization synthesis.